THE GEOLOGICAL SOCIETY OF AMERICA®

Surface slip distributions and geometric complexity of intraplate reverse-faulting earthquakes

Haibin Yang[1,†], Mark Quigley[1], and Tamarah King[1,2]
[1]*School of Earth Sciences, University of Melbourne, Parkville, Victoria 3053, Australia*
[2]*Centre for Observation and Modelling of Earthquakes, Volcanoes, and Tectonics (COMET), Department of Earth Sciences, University of Oxford, Oxford OX1 3AN, UK*

ABSTRACT

Earthquake ground surface ruptures provide insights into faulting mechanics and inform seismic hazard analyses. We analyze surface ruptures for 11 historical (1968–2018) moment magnitude (M_w) 4.7–6.6 reverse earthquakes in Australia using statistical techniques and compare their characteristics with magnetic, gravity, and stress trajectory data sets. Of the total combined (summative) length of all surface ruptures (~148 km), 133 km (90%) to 145 km (98%) align with the geophysical structure in the host basement rocks. Surface rupture length (*SRL*), maximum displacement (*MD*), and probability of surface rupture at a specified M_w are high compared with equivalent M_w earthquakes globally. This is attributed to (1) a steep cratonic crustal strength gradient at shallow depths, promoting shallow hypocenters (~1–6 km) and limiting downdip rupture widths (~1–8.5 km), and (2) favorably aligned crustal anisotropies (e.g., bedrock foliations, faults, fault intersections) that enhanced lateral rupture propagation and/or surface displacements. Combined (modeled and observed) *MDs* are in the middle third of the *SRL* with 68% probability and either the ≤33rd or ≥66th percentiles of *SRL* with 16% probability. *MD* occurs proximate to or directly within zones of enhanced fault geometric complexity (as evidenced from surface ruptures) in 8 of 11 earthquakes (73%). *MD* is approximated by 3.3 ± 1.6 (1σ) × *AD* (average displacement). S-transform analyses indicates that high-frequency slip maxima also coincide with fault geometric complexities, consistent with stress amplifications and enhanced slip variability due to geometric and kinematic interactions with neighboring faults. Rupture slip taper angles exhibit large variations (–90% to +380% with respect to the mean value) toward rupture termini and are steepest where ruptures terminate at obliquely oriented magnetic lineaments and/or lithology changes. Incremental slip approximates *AD* between the 10th and 90th percentiles of the *SRL*. The average static stress drop of the studied earthquakes is 4.8 ± 2.8 MPa. A surface rupture classification scheme for cratonic stable regions is presented to describe the prevailing characteristics of intraplate earthquakes across diverse crustal structural-geophysical settings. New scaling relationships and suggestions for logic tree weights are provided to enhance probabilistic fault displacement hazard analyses for bedrock-dominated intraplate continental regions.

INTRODUCTION

Coseismic ground surface ruptures on faults provide important sources of information on the seismogenic process (Manighetti et al., 2004; Wesnousky, 2008). Surface rupture characteristics (e.g., maximum displacement [*MD*], average displacement [*AD*], and surface rupture length [*SRL*]) may be combined with other seismological parameters to develop earthquake scaling relationships (Allen et al., 2018; Leonard, 2010; Wells and Coppersmith, 1994) for utility in probabilistic seismic hazard analyses (Allen et al., 2018; Stirling et al., 2012) and probabilistic fault displacement hazard analyses (PFDHA; Moss and Ross, 2011; Youngs et al., 2003).

Slip distributions along surface ruptures have been proposed to conform to regular shapes that relate to fracture mechanics, including elliptical shapes (linear elastic theory; Segall and Pollard, 1980), bell shapes (elastic-plastic theory; Cowie and Scholz, 1992a, 1992b), or triangular shapes (off-fault damage theory; Manighetti et al., 2004), although heterogeneous stress distributions may complicate attribution of rupture shapes to a specific theory (Bürgmann et al., 1994). It is still contested whether spatial distributions of coseismic slip and associated shapes are highly variable or self-similar across different spatiotemporal scales, and what the most probable sources of variability may be (Mai and Beroza, 2002; Manighetti et al., 2009). Although standard simplified shapes (e.g., ellipse or triangle) may enable generalized classification of rupture forms, empirical observations show that many ruptures include embedded hierarchical shapes in wavelength and amplitude that are described by self-similar or self-affine geometries (King, 1983; Power and Tullis, 1991). Fluctuations inside the rupture plane may relate to along-strike variations in the fault roughness (Dolan and Haravitch, 2014; Gold et al., 2015; Perrin et al., 2016; Zinke et al., 2014), the rheology of faulted materials (Haeussler et al., 2004; McGill and Rubin, 1999), fault segmentation (Brown and Scholz, 1985; Klinger, 2010; Manighetti et al., 2009; Okubo and Aki, 1987), or fault junctions (Andrews, 1989; Gabrielov et al., 1996; Shen et al., 2009), and/or they may be attributed to the nonlinear, anelastic responses of surficial material to sudden coseismic strain (Gold et al., 2015; Kaneko and Fialko, 2011; Zielke et al., 2015).

The gradient with which fault slip reduces toward rupture termini (i.e., slip taper) may be linked to the interaction with peripheral structures, which may directly affect the earthquake arresting dynamics (Manighetti et al., 2004; Scholz and Lawler, 2004). The slip taper has been suggested to be a scale-invariant property of rocks (Cowie and Scholz, 1992a, 1992b; Scholz and Lawler, 2004). To discern the potential controlling mechanisms of spatial slip gradient variation for both interior segments and termini, more detailed field measurements, maps, and analyses of high-resolution coseismic slip distribution are necessary.

Australian stable continental regions consist of nonextended Precambrian crust (Leonard

†haibiny@student.unimelb.edu.au.

GSA Bulletin; https://doi.org/10.1130/B35809.1; 11 figures; 1 supplemental file.

et al., 2014) that is largely unaffected by active tectonic processes relative to plate boundaries and more rapidly deforming intraplate regions (Johnston, 1989). However, Australia stable continental regions are not immune from seismicity. Since 1968, 11 historical surface-rupturing earthquakes with moment magnitudes (M_w) between 4.7 and 6.6 have occurred in Australian stable continental regions (Figs. 1A and 1B; see King et al., 2019, and references therein). These account for more than half of the instrumented global cratonic earthquakes (Clark et al., 2012; Crone et al., 2003). Studies of the source faults suggest long (i.e., $>10^4$ to 10^5 yr) preceding periods over which no surface ruptures occurred (Clark et al., 2012), which some workers have interpreted as evidence for "one-off" rupture behavior on incipient or "newly formed" brittle faults (Clark et al., 2020; King et al., 2018). Together with the paucity of preceding, historical $M_w > 6$ events on these fault systems (Leonard, 2008; Leonard et al., 2014), this suggests that variations in slip rate, interseismic creep, local-to-regional stress perturbations relating to prior earthquake(s), and fault structural maturity (i.e., the roughness of the fault plane, which is physically scaled to $D^{-0.1}$, where D is the cumulative displacement of a fault; Brodsky et al., 2011) may be of minimal significance in interpreting any slip distribution variability observed in these earthquakes. With the exception of the three surface-rupturing earthquakes on neighboring faults in the 1988 Tennant Creek sequence, which have been explained by proximate Coulomb stress transfer (Mohammadi et al., 2019), 8 of the 11 Australian ruptures are thus considered to be spatially and temporally isolated, with slip distributions that are unlikely to have been strongly influenced by preceding, spatiotemporally proximate earthquakes.

Issues of data handling and measurement uncertainties have been recently addressed by King et al. (2019), who reanalyzed all Australian surface rupture displacements and established new estimates of net-slip metrics that we utilized here. Driven primarily by exploration needs of the natural resources industry, rich and diverse geophysical data sets have also been acquired and are publicly available across the continent (https://data.gov.au/data/dataset/b0f0711d-9763-4041-9fcf-0b40bd1694a5). King et al. (2019) concluded that 90% of Australian surface-rupturing earthquakes have fault orientations that align with prevailing linear anomalies in geophysical (gravity and magnetic) data and bedrock structure (foliations, quartz veins, intrusive boundaries, and/or preexisting faults), but they did not consider the statistical and scaling relationships of surface rupture displacement fields in detail.

In this study, we propose that the shape of surface rupture displacement profiles and the geometric complexity of earthquakes on incipient reverse faults emerging through stable continental region crust are strongly influenced by the relationships among (1) anisotropic structural and geophysical properties of the host crust that provide potential pathways for seismogenic rupture, (2) regional stress trajectories that may be locally influenced by geologic variability, and (3) the depth and dynamics of propagating ruptures that influence how subsurface slip is manifested at the surface. We use net displacements (calculated by trigonometric analyses of vertical and lateral displacements using fault dip estimates) for 10 events from King et al. (2019) and converted surface offsets from the 16 September 2018, M_w 5.3 Lake Muir earthquake (Clark et al., 2020) to net slip assuming pure dip slip and a fault dip of 45°.

Rupture data are compared to the Australian national high-resolution (grid cell size ~80 m) total magnetic intensity (TMI) map (https://pid.geoscience.gov.au/dataset/ga/89596). Since bedrock is exposed at the surface and/or is only thinly (1 to >50 m) blanketed by eolian and/or alluvial sediments (King et al., 2019), TMI signals directly reflect bedrock structures and lithologies in the seismogenic crust. Rock strength properties are not directly measurable by TMI, and so we do not attempt to undertake a detailed TMI analysis to resolve three-dimensional geometries of TMI anomalies. We focused primarily on the azimuthal relationships between surface ruptures and predominant geophysical structural-lithologic lineaments in the TMI data. The azimuthal relationship between geophysical aspects may reveal rock properties that may affect rupture propagation; e.g., lithological boundaries or fault junctions may have lower frictional strength or modulus than intact rocks (Gabrielov et al., 1996). To locate magnetic anomalies above the source without any distortion, a variable reduction to pole was implemented in this database. Intrusive dikes of relatively lower magnetic susceptibility than host rocks have been detected through aeromagnetic mapping in the Yilgarn craton, where they are characterized by lineament anomalies (Dentith et al., 2000, 2009). Magnetic lineaments may represent near-vertical structures such as steep faults, plunging fold axes, or intrusive dikes (Dentith et al., 2009), and these features may act as stress concentrators to become the sites of subsequent faulting (Dentith et al., 2009).

To crudely estimate the subsurface position of rupture with respect to anomalies, we assume planar geometries with uniform dip for vertical geophysical structures. Although hypocentral depths were not resolved in high resolution, most events have centroid moment tensor (CMT) solutions and/or fault models (e.g., from interferometric synthetic aperture radar [InSAR]) with depths of 1–6 km, indicating that the earthquakes studied herein were sourced from shallow fault ruptures (e.g., King et al., 2019, and references therein). The shallow structures could be tracked as short-wavelength responses (magnetic lineaments) in the TMI map. Additionally, national high-resolution gravity data (a grid cell size of ~800 m; https://pid.geoscience.gov.au/dataset/ga/101104) are used to test how the gravitational body forces, which may dominate both the regional and local principal stress direction, might affect rupture complexity. Regional trajectories in maximum horizontal compressive stress (S_{Hmax}) were taken from Rajabi et al. (2017).

GEOLOGICAL SETTING

All historically recorded surface-rupturing earthquakes analyzed here occurred in Australian stable continental regions (Fig. 1A; Clark et al., 2012; Leonard et al., 2014). The Archean Yilgarn craton (Fig. 1A) hosted the Meckering (M_w 6.6, 1968), Calingiri (M_w 5.0, 1970), and Cadoux (M_w 6.1, 1979) events in the Southwest seismic zone (all earthquakes magnitudes in this paper are from Allen et al., 2018), which is one of the four high-seismicity zones in Australia (Leonard, 2008). The Southwest seismic zone (Fig. 1A) also hosted the Katanning (M_w 4.7, 2007) and Lake Muir (M_w 5.3, 2018) earthquakes. The Proterozoic Musgrave block in Central Australia (Fig. 1A) sequentially hosted the Marryat Creek (M_w 5.7, 1986), Pukatja (M_w 5.2, 2012), and Petermann (M_w 6.1, 2016) events. The three Tennant Creek events (Kunayungku M_w 6.2, Lake Surprise West M_w 6.3, Lake Surprise East M_w 6.5, 1988) occurred in the Paleoproterozoic Warramunga Province in the Northern Territory. Geological terrain boundaries are generally not well exposed at the surface but have been inferred from lithological, geochronological, and structure changes (Johnston and Donnellan, 2001); local structures have been mapped by detailed geophysical and geological surveys (Fig. 1C). Detailed descriptions of the geological settings of each studied earthquake were provided by King et al. (2019) and numerous references therein.

OBSERVATIONS

Coseismic Slip Distributions and Rupture Segmentation

Coseismic net slip (Fig. 2) is mainly derived from field measurements of vertical and/or

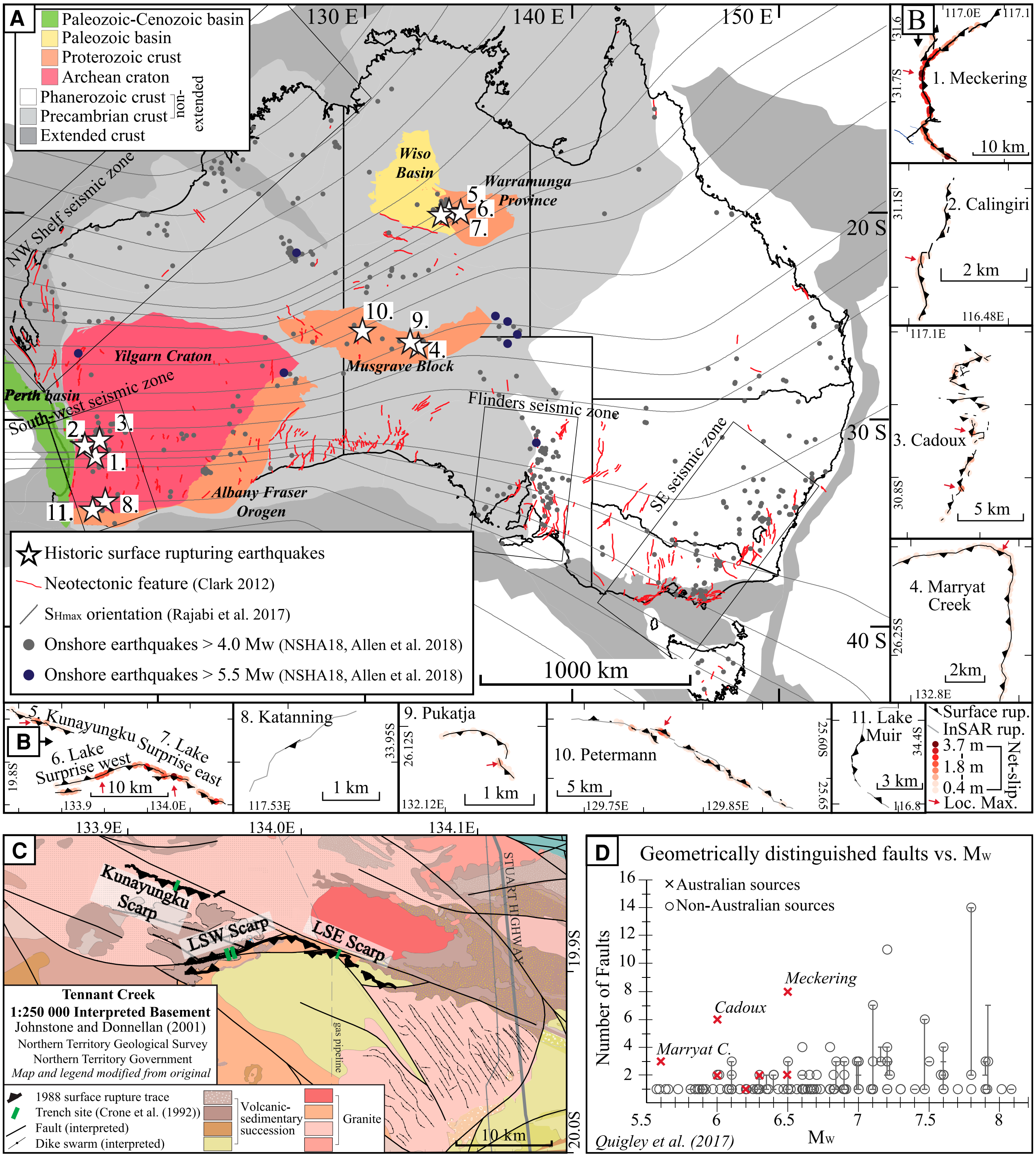

Figure 1. (A) Map of Australia showing sites of historic surface-rupturing earthquakes, geological provinces (Leonard et al., 2014), onshore historic earthquakes >4.0 (1840–2017) (Allen et al., 2018), crustal stress trajectory (Rajabi et al., 2017), neotectonic features (Clark, 2012), and seismic zones (Leonard, 2008). The four rectangular boxes mark four high-seismicity zones in Australia. (B) Maps of surface rupture for each event, numbered chronologically. Dots demonstrate the position of original field measurements, and the color code notes the amount of net slip. Small red arrows note the location of slip maxima for each event. InSAR—interferometric synthetic aperture radar. (C) Interpreted bedrock geology surrounding the Tennant Creek events. The ruptures are aligned with local structures. The legend is simplified to focus on the structures around the surface rupture; for more details, refer to Johnston and Donnellan (2001). Trench locations are from Crone et al. (1992). LSE—Lake Surprise East; LSW—Lake Surprise West. (D) The geometric complexity of rupture segmentation vs. magnitude. Surface-rupturing earthquakes (M_w > 5.5) in Australia are plotted against global compilations (Quigley et al., 2017). Bars denote segmentation ranges of multifault earthquakes based on all reported studies.

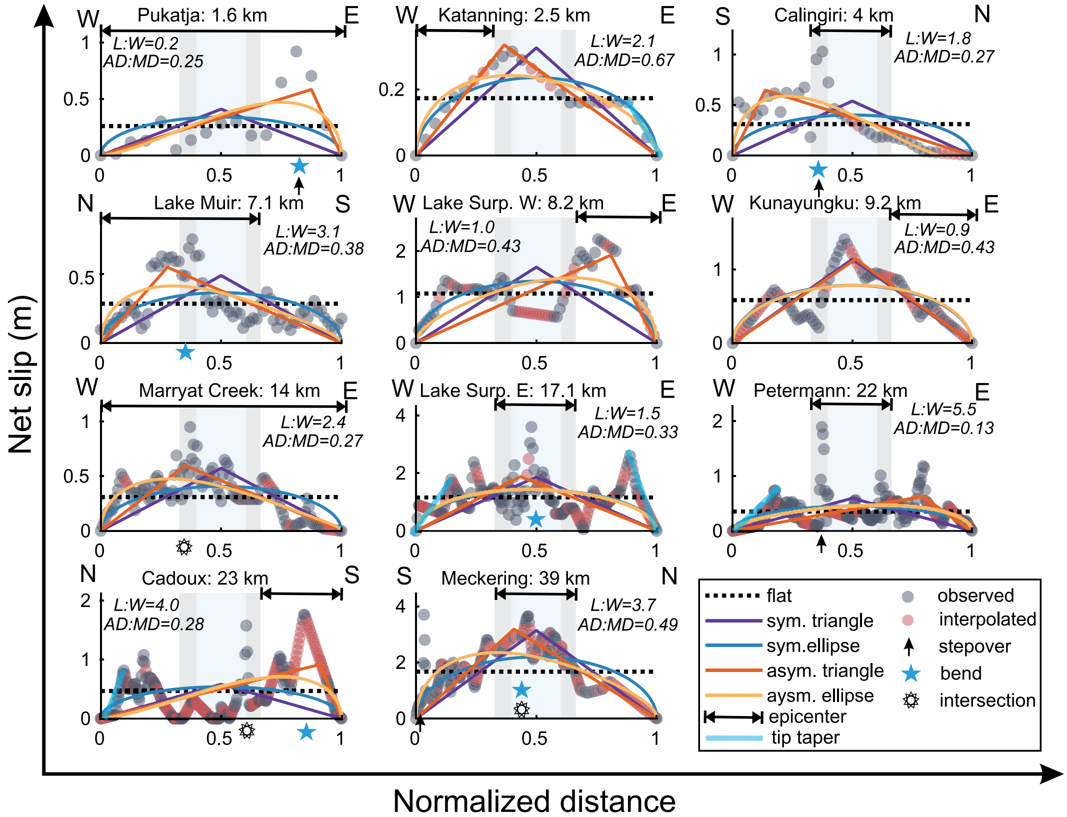

Figure 2. Best-fitting regression curves of different regular shapes to the 11 coseismic displacement profiles in Australian stable continental regions. The events are ordered by rupture length. The distance to the start point is normalized to the rupture length, which is labeled after the name of each event in the title. The filled circles represent the resampled data points, where red color means the resampled point has no original observations within 200 m, while the gray ones indicate the nearest interpolation distance is <200 m. The central quintile ($x = 0.4–0.6$) and central third ($x = 0.33–0.67$) are represented by the faint blue and pink boxes, respectively. The locations of the preferred range of seismic-derived epicenters in each area are projected to fault plane. The epicenter ranges roughly mark the relative position of sources with respect to the central third of the profile. A range across the whole profile means we could not put any preferred range for the corresponding event according to the reported data and uncertainties. The vertical black arrows, blue stars and unfilled stars mark the position of the slip maximum coincident with fault step-overs, bends, and fault intersections, respectively. For the slip taper calculation, we first used the asymmetric (asym) triangular shape function, which may over smooth the slip profile where there are strong perturbations. We corrected those taper angle calculations at ending segments. The thick blue lines are corrections for the rupture tip taper calculation for those ending segments. The rupture length (*L*):width (*W*) ratios and average displacement *(AD)*:maximum displacement *(MD)* ratios are reported for each event. Stress drops (in MPa) reported from the literature ("observed"; see text for sources) and modeled from a logarithmic regression fit to per unit area data ("*modeled*"; see text for details) are: Pukatja (*3.7*), Katanning (20.5, *9.0*), Calingiri (9.0, *6.0*), Lake Muir (*3.3*), Lake Surprise West (13.0, *9.5*), Kunayungku (5.8, *3.8*), Marryat Creek (*1.5*), Lake Surprise East (8.6, *5.9*), Petermann (2.2, *2.7*), Cadoux (2.0, *2.4*), and Meckering (9.0, *4.9*) (Tables S1 and S6 [see text footnote 1]).

lateral discrete surface rupture displacements at surface scarps (Clark et al., 2020; King et al., 2019). Net slip for Katanning was inferred from InSAR data (Dawson et al., 2008; King et al., 2019). Available displacement data for Lake Muir include field, unmanned aerial vehicle (UAV), and InSAR-derived offsets (Clark et al., 2020; Dawson et al., 2008). For this paper, we derive net slip from vertical offsets measured by profiles through InSAR data (Clark et al., 2020), as field/UAV data did not provide full along-rupture coverage.

We investigated the shape of net-slip distributions including the rupture tip taper toward the ends of the faults (termini), and we explored the scaling relationships between average displacement (*AD*), maximum displacement (*MD*), surface rupture length (*SRL*), and magnitude (M_w) (Table S1[1]). Since many profiles were not straight lines but rather highly curved, arcuate, and/or segmented profiles, the *SRL* was taken as the sum of different segments and/or linear approximations of the rupture trace (King et al., 2019; Table S1). Segment boundaries were previously assigned where gaps/steps exceeded 1 km and/or where fault strike varied by >20° in 1 km (Quigley et al., 2017). For major ruptures with parallel segment ruptures (e.g., Splinter segment in Meckering and the segment in Lake Surprise West), the net slip of each segment was projected and added to its major rupture profile.

Here, we describe a "fault step-over" as a location where the most proximate overlapping surface rupture tips are ≥100 m apart, as measured normal to the average orientation of the rupture traces (e.g., Petermann; Fig. 1). A "fault bend" is a location where a change in fault strike along a continuously mapped surface rupture trace is ≥20° (e.g., Pukatja; Fig. 1). A "fault intersection" is a location where two faults with distinctly oriented rupture traces intersect at an angle of ≥20° (e.g., Meckering, Cadoux, Marryat Creek; Fig. 1). Some locations along a rupture trace may be defined as both a bend and a step-over (e.g., Calingiri, Pukatja;

[1]Supplemental Material. Table of all along-rupture net-slip values; document with data tables and figures detailing the data used in our methods, and further details of results. Please visit https://doi.org/10.1130/GSAB.S.13356521 to access the supplemental material, and contact editing@geosociety.org with any questions.

Fig. 2). Details of slip distributions and rupture segmentation have been described further by King et al. (2019).

The Australian earthquake surface rupture patterns are relatively complex when compared with recent global compilations of 135 M_w 4.1–8.1 continental earthquakes (Fig. 1D; Quigley et al., 2017). Rupture complexity is defined by the number of kinematically and structurally distinct fault segments that ruptured in a "single earthquake," which is defined as a continuous seismic energy release with no temporal gaps in seismic moment release rate >20 s. An example of how this modifies previous treatment of these data is the 1988 Tennant Creek earthquake sequence (Fig. 1C), where multiple main shocks and surface ruptures were previously amalgamated into a single event (Wells and Coppersmith, 1994; Wesnousky, 2008) despite the earthquakes occurring several hours apart within a 12 h period and producing independent scarps (Bowman, 1992). Therefore, we treated them as three separate events of $M_w = 6.2$ (Kunayungku), 6.3 (Lake Surprise West), and 6.5 (Lake Surprise East) with their own surface rupture traces (Mohammadi et al., 2019). Three of those $M_w >$ 5.7 events (Cadoux, Meckering, Marryat Creek in Fig. 1D) represent the maximum complexity for corresponding M_w in the global database (Quigley et al., 2017).

Shape, Symmetry, and Slip Taper of Coseismic Slip Distributions

To determine whether surface rupture displacement distributions could be well fit by standard shapes (Bürgmann et al., 1994; Manighetti et al., 2004; Segall and Pollard, 1980), we fit various regression curves to slip data using the fit function (*fit object*) in the MATLAB curve-fitting toolbox (https://www.mathworks.com/products/curvefitting.html). Where large gaps existed between the original observations, we linearly interpolated net slip between the two nearest raw data points. From this, we set a uniform sampling distance of 0.1 km and calculated average displacement (inclusive of interpolated points). Field measurements are coded with gray colors, and interpolated data are coded with red colors in Figure 2.

Following Wesnousky (2008), we fit offset data using a flat line (i.e., *AD*) and symmetric and asymmetric forms of a triangle and ellipse. For symmetric fittings, the apex (modeled *MD*) was located at the rupture midpoint and was the only free variable. For asymmetric triangle forms, the modeled *MD* and its position were free in the regression. For asymmetric ellipse forms, we followed Wesnousky (2008); the shape function was multiplied by a value $(1 - m \times x)$, where x is distance (normalized to rupture length) along the rupture, and m is the variable in regression. The parameter m and the amplitude were two free variables in the asymmetric ellipse function.

We first evaluated goodness of fit using the adjusted R^2, which considers the number of free variables in regression to assess the goodness of fit (Fig. 3A). Adjusted R^2 is correlated with the goodness of fit, where $0.5 \leq R^2 \leq 1$ values are crudely considered to represent a good fit of a specified shape function to the empirical displacement data relative to lower R^2. Because R^2 is not a good independent evaluative measure of goodness of fit for horizontal lines, we also used root mean square error (RMSE) normalized to the mean displacement (*AD*) for each earthquake (Fig. 3B), to enhance our statistical comparison amongst earthquakes of different size. Normalized RMSE decreases with increasing goodness of fit (Fig. 3B).

Asymmetric triangle and ellipse shapes ubiquitously exhibited higher R^2 and lower RMSE relative to their symmetric equivalents because they had more allowable free parameters to enhance the goodness of fit. However, some earthquakes (e.g., Katanning, Kunayungku, Meckering) exhibited high R^2 and low RMSE for all shapes relative to the flat-line *AD* profile ("average" in Figs. 3A and 3B), with small statistical preference toward asymmetric shapes. Other earthquakes were almost equally poorly fit by symmetric, asymmetric, and *AD* shapes (e.g., Petermann, Lake Surprise West, Lake Surprise East); in these instances, displacement profiles could be generalized by the *AD*. Some earthquakes were statistically poorly fit by most or all shapes (e.g., Cadoux, Pukatja) but were best represented by asymmetric triangular fits. The Marryat Creek earthquake was approximately equally well fit by asymmetric triangular and elliptical fits.

We further investigated the symmetry of surface rupture displacement profiles by determining the location of the apex of best-fitting asymmetric triangular and elliptical functions (i.e., the modeled *MD*) relative to the normalized surface rupture half-length (Fig. 3C). Importantly, the location and value of the observed *MD* may differ from the modeled *MD* (e.g., Calingiri, Lake Muir) because the former may be strongly influenced by changes in fault geometry or interactions, while the latter represents a generalized fit to the displacement profile (Fig. 2). Further, if modeled shapes have a low curvature, there may be little significance in the relative position of an apex of the best-fit triangle or ellipse along the rupture profile.

We thus refined our definition of rupture symmetry. "Symmetric ruptures" contained *MD* within the middle third of the rupture trace (light blue and purple shade, Fig. 2) and had best-fitting shape symmetry $\geq$0.33 in Figure 3C. Figure 2 shows $n = 8$ from observed *MD* (73% of total), and Figure 3C shows $n = 7$ (64%) ruptures with best-fitting shape symmetry $\geq$0.33 (Table S2). The Marryat Creek earthquake was counted in the symmetric category. The most symmetric of these (Kunayungku, Meckering, Lake Surprise East; Table S2 [see footnote 1]) had *MD* in the middle quintile of the rupture trace (light blue shade in Fig. 2; symmetry $\geq$0.4 in Fig. 3C). "Asymmetric ruptures" had *MD* in the end thirds of the rupture trace (Fig. 2; $n = 3$ observed *MD*) and best-fitting symmetry values of <0.33 ($n = 4$; Fig. 3C; Table S2). The most asymmetric ruptures were the Pukatja, Calingiri, and Cadoux earthquakes (Fig. 3C). Collectively, when we combined the two different measures of symmetry, 68% of rupture displacement scenarios were symmetric and 32% were asymmetric, which equates to the probability of *MD* (observed + modeled) being located in the $\leq$33rd, 33rd–66th (middle third), and $\geq$66th percentiles of rupture length as 16%, 68%, and 16%, respectively.

We also calculated *AD:MD* ratios (Table S1) for each earthquake, for comparison with global data sets (e.g., Wells and Coppersmith, 1994; Moss and Ross, 2011). These ranged from 0.13 (Petermann earthquake) to 0.67 (Katanning) with a mean of 0.38. The relationships between slip at a discrete location along the *SRL* (e.g., for utility in PFDHA) relative to *AD* and rupture displacement shape are explored further in the Discussion.

The rupture slip taper describes the gradient of decreasing slip toward the terminus of a fault surface rupture trace (Fig. 3D, inset; Scholz and Lawler, 2004). Asymmetric triangle fits may be used to estimate discretized profile-scale slip gradients toward rupture termini. These functions enable good fits to be produced for some profiles, but they may overly smooth the data for some events. This approach minimizes overreliance on individual measurements, which may have low signal-to-noise ratios and misrepresent slip tapers. To refine slip taper estimates for some specific events, we manually fit data using linear regressions to local gradients at rupture termini (thick lines of blue color in Fig. 2), including two termini of the Lake Surprise East event, the right end of the Katanning event, and the left ends of the Petermann and Cadoux events (Figs. 2 and 3D).

We found an anomalously high value of net slip of 1.5 km from the south terminus of the Meckering rupture. We lack confidence in the reliability of the original 1.26 m vertical offset measurement (Gordon and Lewis, 1980) because it is 0.9–1.0 m higher than adjacent

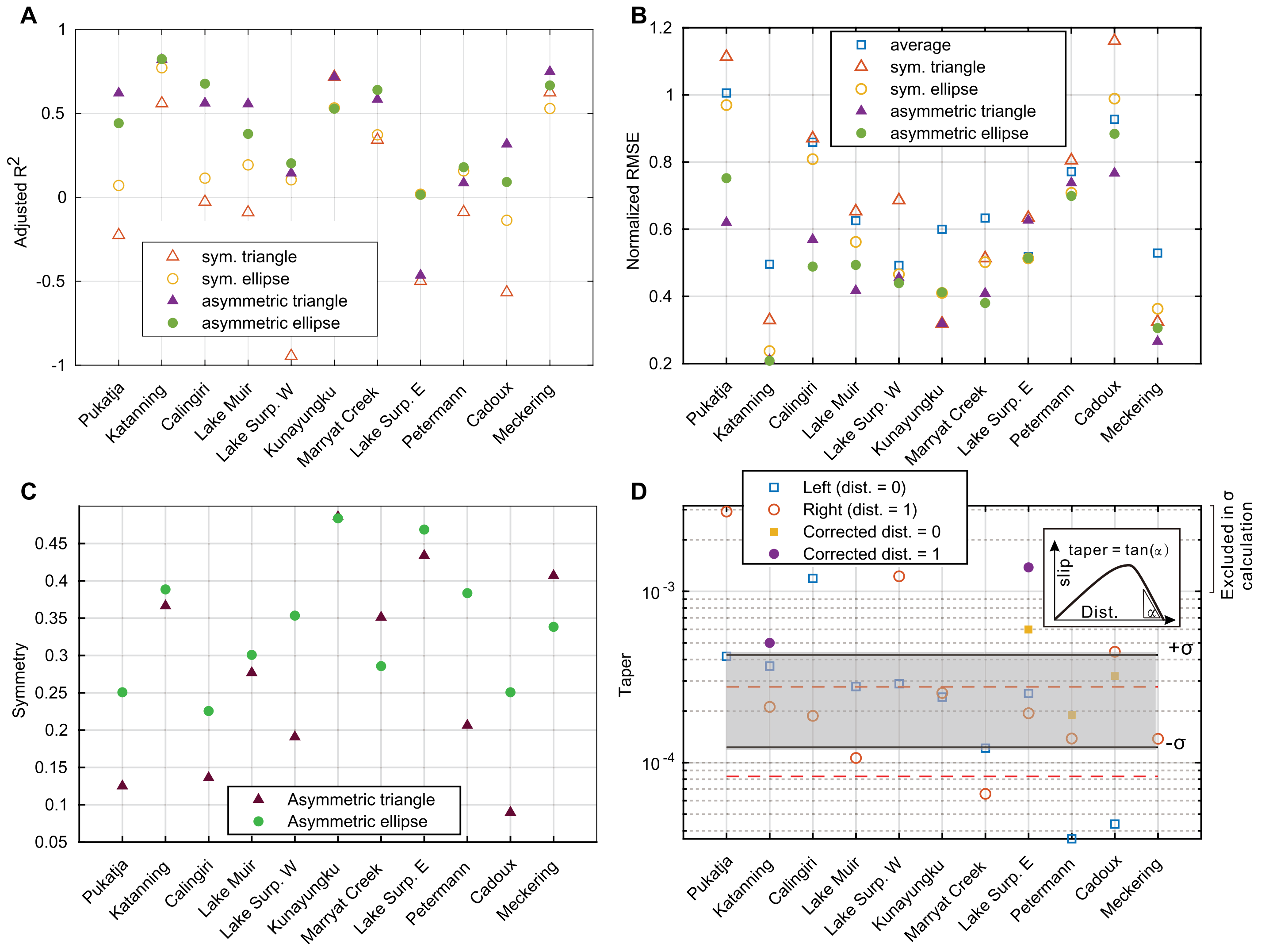

Figure 3. Postanalysis of the fitting results of different shapes. (A) Adjusted R^2 for each shape function regression of all events to evaluate the goodness of the fitting. A higher R^2 value indicates a better-fitting result. (B) Root-mean-square error (RMSE) normalized by the mean value of corresponding measurements. (C) Modeled Symmetry for each event. (D) The rupture tip taper for each event. The insert sketch illustrates the calculation of rupture tip taper, which is defined as the spatial slip gradient when it approaches the terminus. The gray area within two black lines shows 1σ perturbations of the data (excluding four outliers of value >10^{-3}). The perturbation within two red dashed lines is from existing data set for long (>30–100s km) ruptures of strike-slip or normal fault mechanisms (Scholz and Lawler, 2004). Data for each subplot are included in Table S2 (see text footnote 1).

measurements, and our inspection of Shuttle Radar Topography Mission (SRTM) elevation profiles across the projected location of the scarp (http://pid.geoscience.gov.au/dataset/ga/72759) revealed that no scarp of this height is visible (scarp heights of 1–2 m are identifiable elsewhere along the rupture). We therefore excluded this measurement from our slip taper calculation but retained it for *AD* estimations because it contributed only ~1% variance to the *AD* estimate and was thus negligible in statistical effect.

Rupture tip taper results are in the range of 2.7 (±1.5) × 10^{-4} (Fig. 3D). Outliers with anomalously steep tapers were the asymmetric Pukatja (right = east end), Lake Surprise East (both ends), and Calingiri (left = south end) ruptures. Since these slip tapers were calculated for individual earthquakes, the estimates could be compared to "isolated" and "interacting" earthquake tip tapers in the data set of Scholz and Lawler (2004). The average taper value for the 11 Australian earthquakes studied here (2.7 (±1.5) × 10^{-4}) is consistent with (albeit slightly higher than) the reported average value of 1.8 (±0.97) × 10^{-4} for "isolated exterior earthquake tips" near the ends of ruptures that are unlikely to be affected by proximal fault interaction (Scholz and Lawler, 2004). Tip taper outliers from the interacting faults in our study (i.e., the Lake Surprise West and East) are consistent with the Scholz and Lawler (2004) average taper for "interacting exterior earthquake tips" of 1.4 (±1.3) × 10^{-3}.

We acknowledge that the tip tapers described here are all from reverse faults, while those in Scholz and Lawler (2004) were from normal-faulting or strike-slip events. The similar taper estimates suggest that similar slip taper values may be observed across diverse kinematic modes of rupture and may exhibit scale independence. The prevailing characteristics of surface rupture displacement fields (shape, symmetry, slip tapers) relative to the seismological attributes of the associated earthquakes and crustal structure are discussed in more detail in the Discussion.

Seismological Attributes: Epicenter Locations, Source Dimensions, Stress Drops

We estimate a preferred epicenter location along each rupture profile to determine whether any relationships were evident between probable earthquake nucleation locations and slip distributions (Fig. 2). Earthquake epicenters in Australian stable continental regions can have large location uncertainties (i.e., $\geq$5–10 km), particularly for early (pre-1980) and remote events due to the sparse instrumentation of the Australian National Seismograph Network (https://www.fdsn.org/networks/detail/AU/).

Each earthquake studied here has at least three reported epicenter locations. Each reported epicenter was first projected to the nearest surface rupture location, which could be along the fault trace or a fault tip. Where epicentral locations resided at distances >15 km from the rupture plane (e.g., the mislocation of initial epicenters for the Marryat Creek earthquake, which were >30 km from the rupture plane), these events were excluded from the analysis. Revised locations for epicentral locations were used; for example, Denham (1988) and McCue et al. (1987) favored an epicentral location for the Marryat earthquake on the east-west–oriented (W) branch (Fig. 2). We counted the number of epicenters that projected to each third of the rupture length and considered the rupture third with the most projected epicenters (or best-constrained epicenter locations; e.g., we preferred the epicenter locations and associated uncertainties for the Tennant Creek earthquakes of Choy and Bowman, 1990) as the favored host third of the epicenter (horizontal double-arrowed lines in Fig. 2). If the preferred epicenter location was proximal to a boundary between adjacent rupture thirds, we included both thirds as possible hosts for the epicenter. King et al. (2019) presented a detailed discussion of the epicenters associated with each earthquake.

The epicenter positions that we display in Figure 2 are the preferred host third(s) based on all reported epicenter data for each earthquake. A "unilateral" rupture (e.g., Katanning, Lake Surprise West, Kunayungku, Cadoux; Table S2) is defined as containing the projected earthquake epicenter in either of the end thirds of the rupture trace, and a "bilateral" rupture (e.g., Calingiri, Lake Surprise East, Petermann, Meckering; Table S2) contains a projected epicenter in the middle third of the rupture. Where the projected location of the epicenter onto the rupture trace was insufficiently precise to enable designation into a specific third of the rupture (Pukatja, Marryat Creek, Lake Muir; Table S2), we did not consider it in the analysis of rupture directivity. We did not examine the vertical component of rupture propagation. Of the eight ruptures analyzed, 50% exhibited unilateral and 50% exhibited bilateral rupture directivity, and no relationship between rupture shape and epicenter location was evidenced.

The hypocenters for all events are subject to large locational uncertainties (>5 km) due to large distances between the instrumental networks (particularly pre-1980) and earthquake locations (Leonard, 2008). However, revised hypocenter estimates are available for most events (excluding Katanning, Pukatja, and Petermann; Table S4 [see footnote 1]). Additionally, CMT depth results (location of predominant moment release) and modeled faults (e.g., InSAR inversion) are available for some faults (Table S4). These hypocentral, centroid, and fault-depth estimates have a combined mean depth of 3.6 ± 1.9 km, while revised hypocenters have mean depths of 4.4 ± 2.1 km. These estimates are significantly shallower than reverse-faulting earthquakes in the noncratonic areas outside Australia, which have a mean depth of 14 ± 5 km (Wells and Coppersmith, 1994; Wesnousky, 2008). We did not consider the contribution of additional (epistemic) uncertainties for this data set but note that shallow hypocenters are further required in the Australian examples to balance seismic moments against rupture area constraints.

We estimated downdip rupture widths (*W*) by averaging the results of four width estimates (Table S3 [see footnote 1]) based on (1) hypocenter/CMT/fault depths with dip of 45°, (2) same depth as (1) with preferred dips from King et al. (2019), (3) revised hypocenters (excluding Katanning, Pukatja, and Petermann; see Table S4) with dip of 45°, and (4) same depth as (3) with preferred dips from King et al. (2019) (all results are given in Table S5 [see footnote 1]).

The *SRL:W* ratios were estimated from our preferred widths and are shown in Figure 2 (*SRL* is abbreviated to *L* in Fig. 2). Width (*W*) ranged from 1.2 km (Katanning) to 11.6 km (Lake Surprise East). *SRL:W* ratios ranged from 0.2 (Pukatja) to 5.5 (Peterman), with an average *SRL*:*W* of 2.4. These are generally consistent with the range of *SRL:W* ratios in global compilations of dip-slip earthquakes over the same M_w range (0.7–4; average 1.5; Weng and Yang, 2017). *SRL:W* ratios exceeded 2.0 in 55% of events. The three earthquakes with longest *SRL* yielded the three largest *SRL:W* ratios. The variability in *SRL:W* ratios in this small data set can be considered high when compared with global data.

Stress drops have been reported for several of the earthquakes studied here (Fig. 2 caption). It is critical to first acknowledge that stress drops can be estimated via a variety of methods, including (1) static shear stress drop ($\Delta\sigma^s$) from established equations (e.g., Starr, 1928), which include average fault displacements (e.g., ~9 MPa for Meckering and Calingiri; Denham et al., 1980), and (2) dynamic stress drops estimated from source time functions (e.g., ~5.8–13 MPa for the Tennant Creek earthquakes; Choy and Bowman, 1990). Second, stress drop estimates are highly sensitive to estimates of rupture size and slip, and variations in fault rock shear strength, and they are therefore accompanied by large (and typically uncharacterized) uncertainties both in absolute value and in spatial distribution (Dawson et al., 2008; Denham et al., 1987). Third, stress drops have not been established for all earthquakes studied here, and thus there is epistemic uncertainty in how to compare one earthquake with another in this aspect. The highest reported $\Delta\sigma^s$ estimates are 14–27 MPa for the Katanning earthquake (Dawson et al., 2008), and the lowest (~2 MPa) are for the Petermann and Cadoux earthquakes (Attanayake et al., 2020; Denham et al., 1987; Table S1). Given these uncertainties and variance, ensemble modeling of stress drops using a variety of source fault characteristics and other input parameters was warranted.

We modeled $\Delta\sigma^s$ for all earthquakes by averaging the results from four stress drop estimates, which included: the method from Madariaga (1977) using seismic moment M_O (estimated from M_W), *W*, and fault area (assuming an elliptical fault); the method of Griffith et al. (2009) based on Madariaga (1977) using *AD*, *W*, and *L*, with 20 GPa and 50 GPa shear modulus (μ) (Zhao and Muller, 2003); and published stress drops (Table S1). The full results of these estimates are detailed in Table S6 and Figures S1 and S2 (see footnote 1).

Our $\Delta\sigma^s$ values ranged from 1.5 ± 0.9 MPa (Marryat Creek) to 9.5 ± 5.9 MPa (Lake Surprise West) with a mean of 4.8 ± 2.8 (1σ) MPa. These values vary from previously reported $\Delta\sigma^s$ values (Table S1) by 21% (Cadoux) to 56% (Katanning). (Note that our calculations incorporated these previously published data.)

Cratonic in situ stresses have relevance to discussions on the seismological characteristics of these earthquakes. Proxy measurements of stresses at 0–1.5 km depth (and extrapolation to greater depths) imply large increases in maximum horizontal and deviatoric stresses from the surface (~5–20 MPa) to ~1.5 km depth (~100 MPa; Bamford, 1976) and to depths of ~5 km (~>200 MPa; Denham et al., 1980). The possibility that stress drops exhibit an aspect of depth dependence is considered in this context (Huang et al., 2017).

S-Transform Analysis of the Slip Residuals

Earthquake slip distributions commonly exhibit aspects of hierarchical self-similarity or self-affinity (Frankel, 1991; King, 1983; Mai and Beroza, 2002), which manifest as low-amplitude and short-wavelength features (i.e., low-level shapes) embedded into the high-amplitude and long-wavelength first-order shape of the total displacement field (i.e., the basic shape).

To investigate the spectral characteristics and distributions of low-level shapes, we first subtracted the basic shape component from the discrete observations and applied S-transform analyses on the residuals (Stockwell et al., 1996). The basic shape (triangle or ellipse) was selected by the shape fitting with higher R^2 (Fig. 2). The S-transform is based on the idea of the continuous wavelet transform and has a moving and scalable localizing Gaussian window. The advantage of the S-transform is that it can deal with nonstationary signals (like the slip distributions in this study) and provide a clear space-frequency representation of the slip distribution, which is not available in the classical Fourier spectrum method.

The S-transform given by Stockwell et al. (1996) is expressed as

$$S\left(l,k\right)=\int_{-\infty}^{\infty}h\left(x\right)\frac{\left|k\right|}{\sqrt{2\pi}}e^{-\left(l-x\right)^{2}k^{2}}e^{-i2\pi kx}dx, \quad (1)$$

where S is the S-transform of the space function $h(x)$, which is the residual spatial distribution; k is the spatial frequency, and l is the parameter that determines the position of the Gaussian window. The window size is inversely scaled with k. The S-transform characterizes the local spectrum, and averaging the local spectra over the whole space gives the Fourier spectrum as

$$\int_{-\infty}^{\infty}S(l,k)dl=H(k), \quad (2)$$

where $H(k)$ is the Fourier transform of $h(x)$. In this study, $h(x)$ of each event was normalized by the corresponding maximum residual. In the following, we first demonstrate the frequency-space distribution, $S(l,k)$, of the residual signals, and then we check its averaging representations, $H(k)$. Potential sources of sampling bias are that some fault segments have fewer measurements relative to others, and that the slip shapes derived for the faults with sparse measurement data may be oversimplified.

Figure 4 shows the results of the S-transform analysis. The spatial frequency parameter k is a discretized value of *SRL*/the wavelength of the specified increment. For example, a value of $k = 50$ is equal to a wavelength of 280 m for the Marryat Creek earthquake (*SRL* = 14 km) and 780 m for the Meckering earthquake (*SRL* = 39 km). A value of $k = 0$ represents a rupture shape wavelength >1.5 *SRL* with an infinite upper limit representing a horizontal line (i.e., residuals that are collectively fit by a shape with a wavelength longer than *SRL*). A value of $k = 1$ is equivalent to fitting the displacement profile with one shape (wavelength = *SRL*). As the uniform resampling interval is 100 m, the highest spatial frequency that can be recovered is 200 m. The z axis is a unitless measure of the relative apportionment of energy (i.e., probability distributions) for different residual wavelengths (i.e., spatial frequencies) plotted as discrete (100 m) increments along the *SRL*. Since the range of computable values for k is conditional upon *SRL* and the minimum wavelength of the sampling interval, larger values of k can be estimated for longer ruptures (e.g., Meckering, Petermann) relative to short ones (e.g., Pukatja, Calingiri).

Figure 5 shows the averaged S-transform results for $H(k)$ over the whole rupture length (Table S2). The Pukatja earthquake exhibits minimal statistical preference amongst $k = 1$–4. This is consistent with (1) the highly sinuous and structurally complex surface rupture morphology, which could promote slip variability (manifested as embedded shorter-wavelength shapes in the general profile), and (2) the high density of surface displacement measurements, which could enhance recognition of any displacement variability (Clark et al., 2014). Enhanced high-frequency energy at $4 \geq k \geq 8$ in the eastern third of the rupture is associated with the location of peak displacement and variability at a step-over (Figs. 1 and 4).

The Katanning earthquake exhibits clear statistical preference for $k = 1$, with small signals associated with $k = 0$ (suggestive of adherence to a broader form) and $k = 2$ and 3 toward rupture termini (Fig. 4), where small fault orientation changes are possible based on InSAR data (Fig. 1; Dawson et al., 2008), and where enhanced variability would be expected as deformation was diffused from the primary fault. This earthquake exhibits the simplest S-transform spectra and is consistent with a shallow-focus, circle-shaped, structurally simple rupture (Dawson et al., 2008), although these data also reflect the utility of our INSAR-derived rupture model, given the lack of discrete field-observed surface displacements.

The Calingiri earthquake exhibits a statistical preference for $k = 3$ (and $k = 2$) above $k = 1$, consistent with the segmented rupture trace (Fig. 1) and deformation undulations at wavelengths of ~1.3–2 km (Figs. 2 and 5B). The zone of enhanced high-frequency energy ($8 \leq k \leq 15$ corresponding to wavelengths of 500–260 m; Figs. 4 and 5B) is concentrated in the southern half of the rupture and is coincident with maximum displacement at a fault step-over (Figs. 2 and 4).

The Lake Muir earthquake exhibits statistical preference for $k = 2$ (and $k = 3$) corresponding to wavelengths of 2.4 (and 3.6 km). The preference of a segmented rupture is consistent with distinctive trends in the rupture trace with ~20°–45° variance (Clark et al., 2020). Embedded shorter-wavelength triangular shapes (Fig. 2) were identified at $6 \leq k \leq 9$ (1.2–0.8 km wavelength; Figs. 4, 5A, and 5B), and these included additional hierarchies of embedded energy undulations at higher k (Fig. 4). High-frequency energy signals coincide with peak displacement at a small fault step-over, and a change in average rupture trace orientation (fault bend), in the eastern half of the rupture (Figs. 1 and 2; Clark et al., 2020).

The source ruptures of the 1988 Tennant Creek share similar attributes: (1) a clear statistical preference for low k ($k = 1$ for Lake Surprise West and East; $k = 2$ for Kunayungku), with progressively decreasing contributions with increasing k (which are particularly distinct when compared to the similarly sized Marryat Creek and Petermann earthquakes; Figs. 4, 5A, and 5B), (2) localized pulses of energy at high k in the central portions of rupture traces (all), coincident with peak displacements that may be associated with fault bends and/or intersections (Lake Surprise East; Figs. 1 and 4), and (3) minimal energy contributions from wavelengths <3 km (Fig. 5B). In comparison, the Marryat Creek and Petermann earthquakes are characterized by (1) large mean energy contributions at $k \geq 5$ in Figure 5A (wavelength ~2–3 km) that are similar to the mean relative probabilities at $k = 1$ or 2 (Fig. 5A), and (2) localized high k (>10) peaks (~1 km wavelengths; Fig. 4) coincident with maximum displacement domains at fault intersections (Marryat Creek) and step-overs (Petermann; Figs. 1 and 2). In addition to the distinctions, it is notable that the Lake Surprise East and West and Petermann earthquakes exhibit less definitive shape profiles that are almost as well represented by average displacements (flat lines) as triangular or elliptical fits, whereas Kunayungku and Marryat Creek adhere more closely to asymmetric triangles.

The Cadoux earthquake is statistically best-defined by a single ($k = 1$) asymmetric triangle displacement profile (Figs. 2, 4, and 5) despite a highly complex and segmented ($n = 6$ faults;

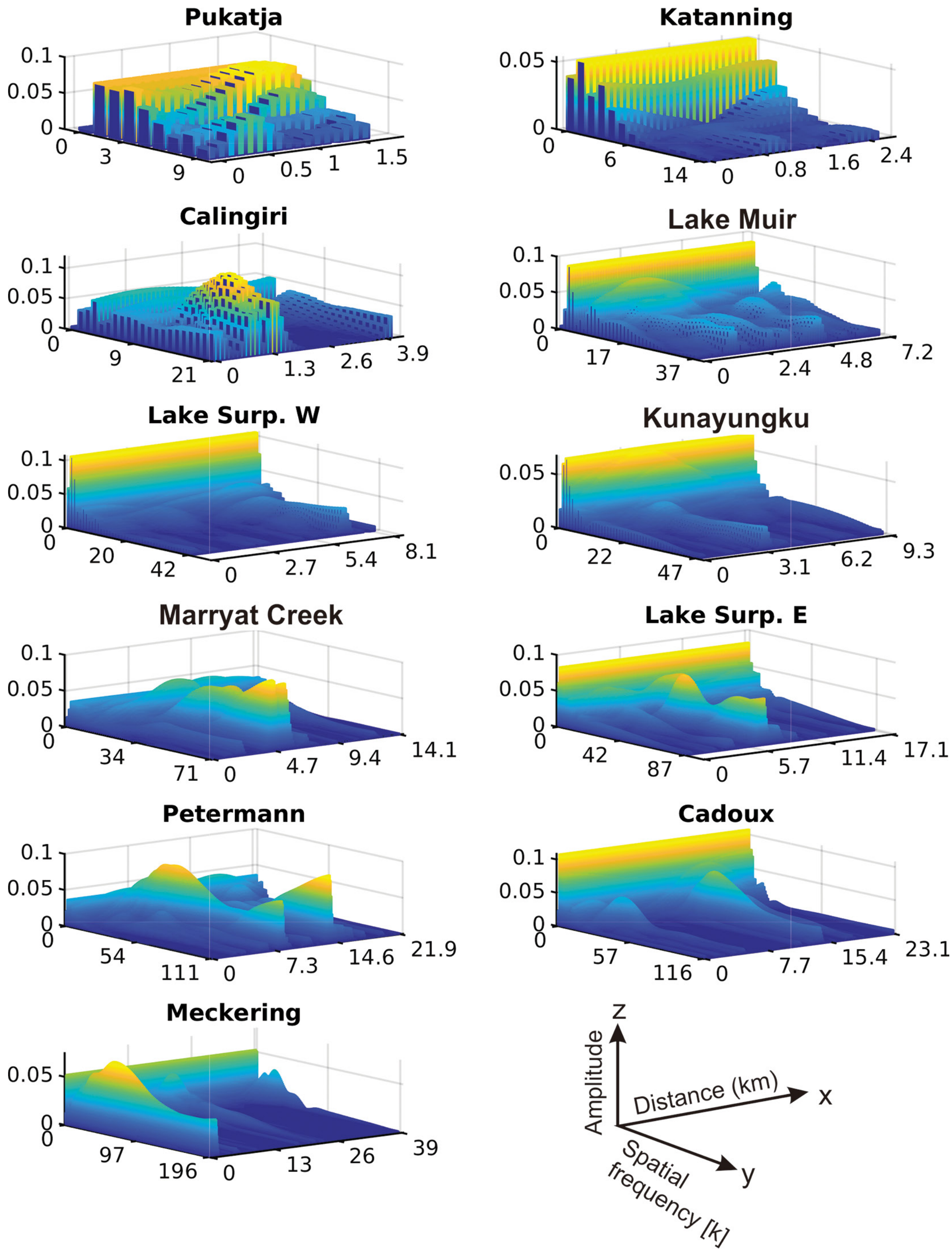

Figure 4. S-transform analyses for the residuals of the best-fitting regression curves for different shapes. The dominating spatial frequency is generally less than 5, but there are significant high-frequency signals for Calingiri (at x = ~1.3 km), Marryat Creek (at x = ~5 km), Lake Surprise East (at x = ~7 km), Petermann (at x = ~8 km), and Cadoux (at x = ~14 km).

King et al., 2019) rupture trace (Fig. 1), suggesting strong transfer of vertical displacement across complex fracture networks. Both the northern and southern thirds of the rupture include local slip maxima at high-angle fault intersections (Figs. 1 and 2) and high k spikes associated with embedded high-frequency triangular shapes (Fig. 2). Distinct from Lake Surprise West and Kunayungku, there is a persistent mean probability signal at $2 \geq k \geq 10$ (Fig. 5), the upper range ($k = 5$–10) of which corresponds with wavelengths of 4.6–2.3 km.

For the Meckering earthquake, we analyzed the full published data set, without removing the anomalously high net-slip value previous discussed in the southern part of the rupture. The Meckering earthquake exhibits consistent relative probabilities for $k = 1$ and $k = 2$, both of which are statistically preferred in the $0 \geq k \geq 10$ range (Fig. 5). A high k spike was observed for the southernmost end of the rupture (Fig. 4). The persistent signal at $4 \geq k \geq 10$ (Figs. 5A and 5B) corresponds to contributions from ~9.8–3.9 km wavelengths; these are evident as hierarchical, self-similar triangle-shaped features embedded within the overall triangular-shaped slip shape (Fig. 2). The Meckering earthquake could have included as many as 4–8 planar faults (Fig. 1D), consistent with elevated signals at $k \geq 4$. No evidence for fault trace orientation changes or fault

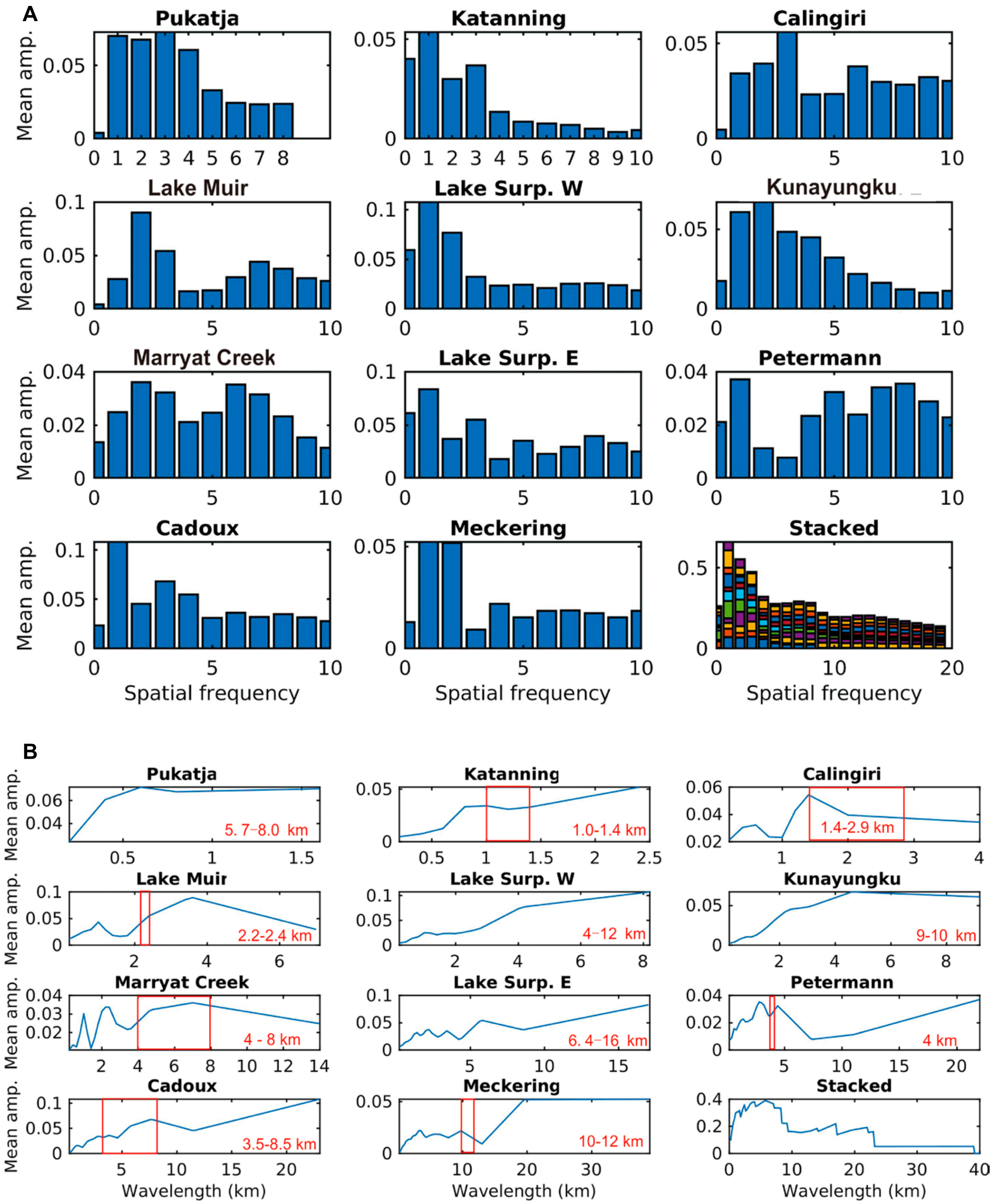

Figure 5. Averaging amplitude of the S-transform results versus the spatial frequency (A) and wavelength (B) over the whole domain for each event. (A) Only those spatial frequency signals lower than 10 are shown here because the averaging method would smooth out those high-spatial-frequency signals, and the mean amplitude quickly decreases with spatial frequency after the dominating spatial frequency (i.e., 1–3), especially for the stacked case. (B) Spatial frequency converted to wavelength with the rupture length. The downdip rupture width is noted for each event and is also marked with a red box in the *x*-axis for those events with surface rupture length (*SRL*):width (*W*) > 1. The mean amplitude of the S-transform results generally decreases with the wavelength, but some events have large contributions from short-wavelength signals (<~5 km), which are comparable with the downdip rupture width for those relatively shallow events.

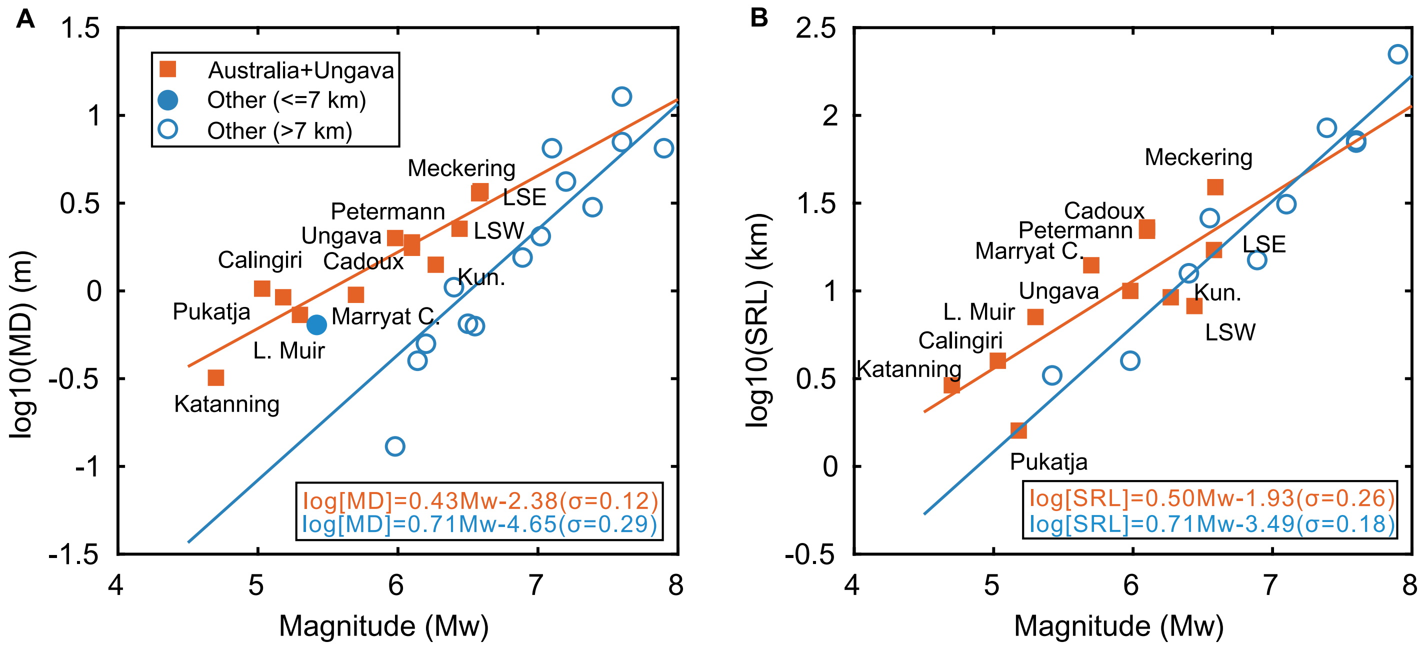

Figure 6. Comparison of the maximum displacement *(MD)* (A) and surface rupture length (*SRL*) (B) versus magnitude scaling relationship for thrust earthquakes between nonextended cratons in Australia and Ungava (Canada) and other areas (Moss and Ross, 2011; Wells and Coppersmith, 1994). Solid lines correspond to the linear regression results for the two groups. Values of slip maxima and rupture length in Australia are estimated to be higher than global comparatives. LSE—Lake Surprise East; LSW—Lake Surprise West.

intersections on displacements was found; the displacement profile was statistically well fit by the triangular shape function (Fig. 3).

MD, *SRL*, and Fault Geometry

We plotted *MD* and *SRL* against M_w (Fig. 6) and compared the results against global thrust fault regressions from Wells and Coppersmith (1994) and Moss and Ross (2011). The 1989 Ungava, Canada, earthquake (Adams et al., 1991) also occurred in a nonextended craton and was included with the Australian events for our linear regression analysis. Regression equations are given in Figure 6. For events of $M_w < 7$, the linear regression fitting shows that both the *MD* and *SRL* values in nonextended cratonic areas are higher than global comparatives (Fig. 6). The large *SRL* for stable continental region earthquakes compared to analogous M_w global earthquakes was also reported by Clark et al. (2014).

Wells and Coppersmith (1994) found that the *SRL* is typically ~75% of subsurface rupture length. However, balancing M_w against *AD*, *L*, and shallow downdip rupture width (i.e., rupture area), and considering aftershock distributions with respect to *SRL*, results suggest that *SRL* ≈ subsurface rupture length in the Australian stable continental region earthquakes studied here. For example, the precisely located aftershocks of the Petermann earthquake enabled us to map a maximum subsurface rupture length that is ≈*SRL* (Attanayake et al., 2020). This may be attributed to the shallow earthquake ruptures in bedrock that extend to the surface without significant influence of thin sediments.

Following our descriptions of fault stepovers, bends, and intersections above, we compared the locations of observed *MD* against these fault geometric aspects. *MD* for the Petermann coincides with a fault step-over (Figs. 1 and 2). *MD* for Pukatja, Lake Surprise East, Calingiri, Cadoux, and Lake Muir coincides with fault bends (Figs. 1 and 2) and, in the case of Pukatja and Calingiri, small stepovers in the rupture trace. *MD* for Meckering and Marryat Creek coincides with fault intersections (Figs. 1 and 2). Fault geometries in the regions of *MD* on the Kunayungku, Lake Surprise West, and Katanning surface ruptures can be considered sufficiently homogeneous to not require classification into the geometric categories described above. In summary, *MD* occurs proximate to or directly within zones of enhanced fault geometric complexity (as evidenced from surface ruptures) in 8 of 11 earthquakes (73%), and *MD* can be approximated by 3.3 ± 1.6 (1σ) × *AD*.

Probability Distribution of Coseismic Slip

The probability distribution of coseismic slip was suggested to be a proxy of stress distribution and fault strength by Thingbaijam and Mai (2016), who undertook probability analysis by using subsurface coseismic slip data. Due to the limited data set of surface coseismic slip, especially for those earthquakes of $M_w < 6$, we only analyzed the probability distribution of coseismic slip for two end-member cases of Meckering and Petermann, for which the surface rupture geometry showed significant differences in distribution and shape (Figs. 1 and 2).

With the uniformly sampled (0.1 km) coseismic slip data, we first counted the bins of slip value in corresponding ranges; then, we measured the complementary cumulative distribution function (1–*F*[*u*]), which was fit by the exponential function, $e^{(-u/u_h)}$, and the truncated exponential function, $\frac{e^{(-u/u_c)} - e^{(-u_{max}/u_c)}}{1 - e^{(-u_{max}/u_c)}}$, where u and u_{max} are the coseismic slip and the maximum slip, respectively, and u_h and u_c are the unknown rate parameters used in the regression for the exponential function and truncated exponential function, respectively. In the case of the truncated exponential function, we also defined u_t, which denotes the position where the probabilities start to deviate from an exponential trend (Fig. 7). Both u_h and u_c are related to the expected value of the distribution, but u_c is likely to be larger than the maxima of the distribution, and the physical implications of different u_c are discussed later. The goodness of fit is measured by R^2.

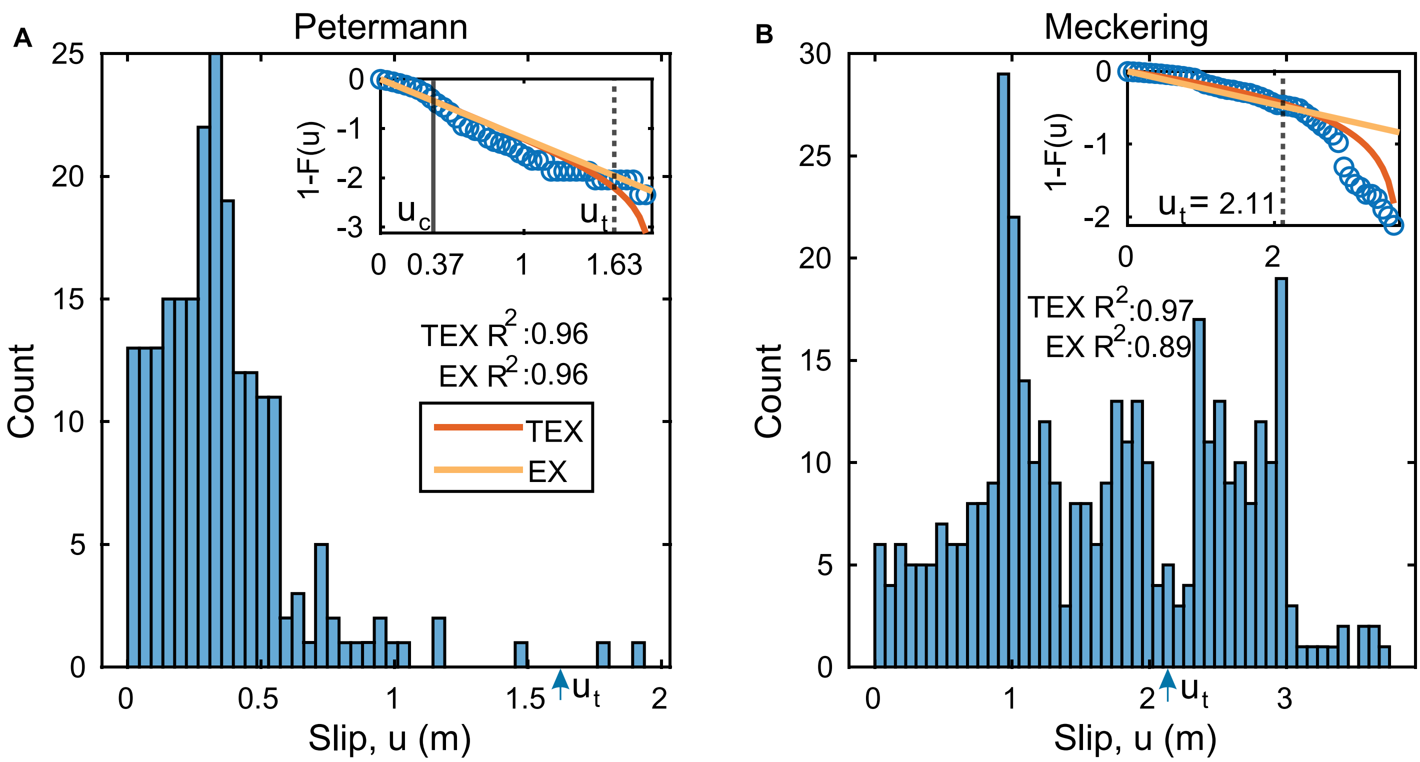

Figure 7. Histograms of coseismic slip for the Peterman (A) and Meckering (B) earthquakes. The insert plot shows the complementary cumulative distribution function (1–*F*(*u*)), which is fit by exponential functions (EX) and truncated exponential functions (TEX). The fitting result is measured by R^2. The Petermann earthquake demonstrates a near-critical behavior, while the Meckering earthquake demonstrates a subcritical behavior. Here, u_h and u_c are the unknown rate parameters in the regression. In the case of the truncated exponential function, u_t is the position where the probabilities start to deviate from an exponential trend.

The Meckering event is best fit by the truncated exponential function, while the R^2 is the same for both fitting functions in the case of Petermann earthquake (Fig. 7). The Meckering and Petermann cases represent two end-member cases listed in Thingbaijam and Mai (2016): $u_c > u_t$ (subcritical behavior in the Meckering event, where u_c is larger than u_{max}; not shown in Fig. 7B) and $u_c < u_t \approx u_{max}$ (near-critical behavior in the Petermann event, where u_t is close to u_{max}; thus, both fitting functions produce close R^2 values). These end members describe fault rupture propagation that has to overcome strong physical constraints during rupture (subcritical) versus weak physical impediments to rupture (near-critical).

The subcritical behavior observed for the Meckering event is suggestive of a spatially variable coseismic stress drop (including relatively high and low components) due to rupture on crustal structures that are variably oriented with respect to S_{Hmax} (Figs. 1 and 8) and that require complex kinematic and geometric interactions to enable rupture propagation. This may ultimately favor a triangular shape for the slip distribution. Conversely, in the Petermann earthquake, the relatively straight, simple, and "weak" source fault (related to inherited bedrock structure) and high-angle relationship with respect to S_{Hmax} and gravity gradient may favor a more uniform displacement (low-curvature) shape, albeit with localized complexity at a fault step-over (Fig. 1).

Comparison of Rupture Orientations with Crustal Geophysical Properties

Surface rupture traces are plotted on aeromagnetic intensity maps in Figure 8 and on Bouguer gravity contour maps in Figure 9. Additional rupture characteristics (stress drops $\Delta\sigma^s$, discretized surface rupture orientations with respect to S_{Hmax}) are shown in Figure 10 and compared to geophysical setting below.

All earthquakes similarly exhibit rupture traces that clearly align with prevailing magnetic structures (King et al., 2019). The Petermann earthquake surface rupture parallels the predominant NW-trending orientation of regional magnetic structure (Fig. 8) and is parallel to NW-striking, NE-dipping bedrock foliations at the surface (Attanayake et al., 2020; King et al., 2019). Magnetic fabrics continue in rupture-parallel orientations beyond the rupture termini, although minor curvature is evident at the NW end; no high-angle geophysical structures that could act as barriers to rupture were identified. The Pukatja surface rupture trace parallels the edge of a strong magnetic contrast. The Marryat Creek ruptures are subparallel to E-W– and NNE-trending lineament sets. The three Tennant Creek ruptures parallel NW and approximately E-W lineaments, geological contacts, and previously mapped faults (Fig. 1C). The complex array of surface rupture traces in Cadoux parallels magnetic fabrics oriented NW, NE, and E-W to ENE-WSW. The northern and southern sections of the Meckering rupture parallel NE- and NW-trending magnetic lineaments, respectively; the central N-S–striking rupture coincides with a less well-defined but still identifiable zone of changes in magnetic structure and intensity. Katanning parallels NE-trending lineaments. The Calingiri rupture parallels N-trending lineaments (Fig. 8). Clark et al. (2020) concluded that the Lake Muir rupture trace parallels preexisting structures evident as N- to NE-trending surface features (valleys) that parallel minor lineament trends in the magnetic data; the bedrock structural controls on Lake Muir are amongst the least obvious in our data set.

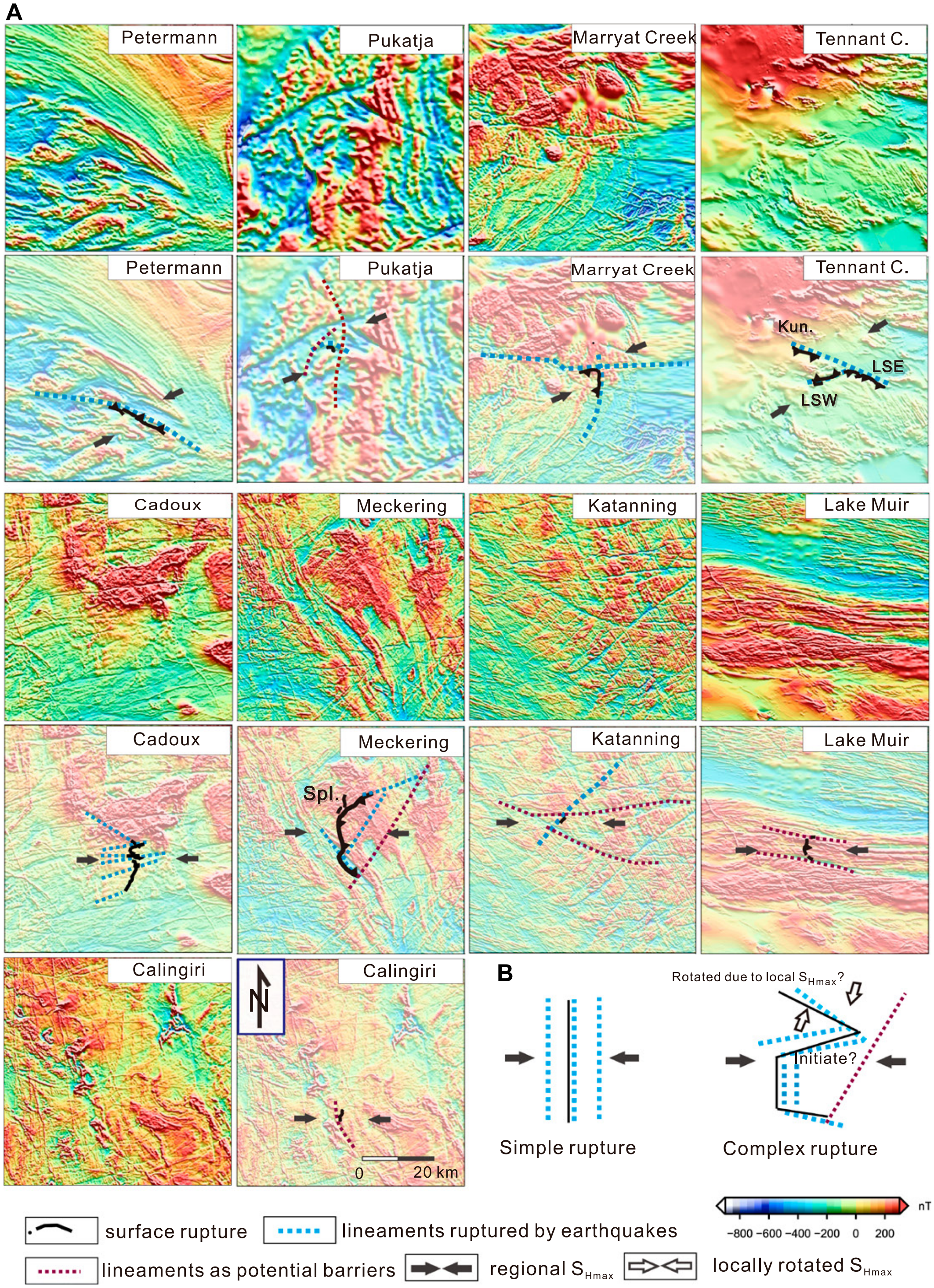

Figure 8. (A) Total magnetic intensity map showing how lineaments affect the development of surface ruptures. The uninterpreted map is put adjacent to the interpreted map. Based on the regional S_{Hmax} orientation, the 11 events are divided into two groups: (1) the Petermann, Pukatja, Marryat Creek, and Tennant Creek events with an average azimuth of 21°–32°, and (2) the Cadoux, Meckering, Calingiri, Katanning, and Lake Muir events with an E-W–oriented S_{Hmax}. The area in each subplot has the same scale of 0.6° × 0.6°. Spl. in Meckering is short for the secondary Splinter rupture. (B) Sketch model illustrating how the orientation of S_{Hmax} with respect to lineaments (weak zones) may affect the surface rupture complexity.

Of the total combined (summative) length of all surface ruptures (∼148 km), we estimate between 133 km (90%) and 145 km (98%) align with geophysical structure in the host basement rocks (Fig. 8). In instances where one orientation of magnetic fabric is clearly dominant in the host bedrock (e.g., Petermann, southern part of Marryat Creek, all Tennant Creek earthquakes), the entire rupture trace is parallel to that fabric. Where two or three sets of magnetic fabrics are present, ruptures may involve all fabrics (e.g., Marryat Creek, Cadoux, Meckering) or remain confined to a single trace that is parallel to one fabric and truncated by distinct high-angle fabrics (e.g., Katanning, Calingiri).

Type Classification Scheme for Earthquakes Based on Crustal Structure and Rupture Characteristics

Type 1

The straightest (i.e., smallest range in incremental orientations; Fig. 10A; classified as “type 1” ruptures) and least segmented

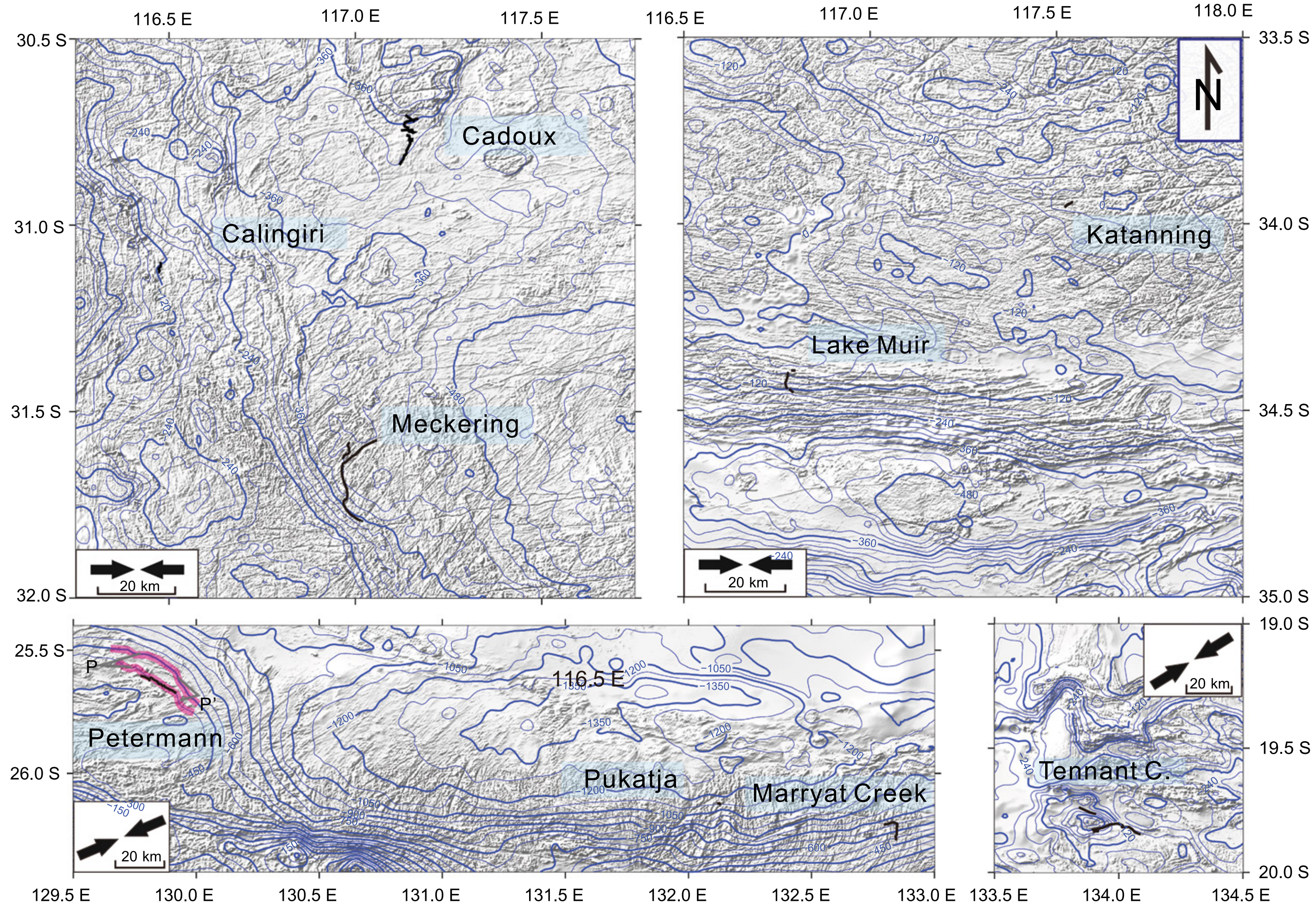

Figure 9. (A) Bouguer gravity anomaly (unit: µm s⁻²) contours overlying the shading map of magnetic lineaments. Surface ruptures are drawn with black lines, and their names are labeled adjacent to the rupture. Black arrows show regionally averaged S_{Hmax}. Red thick lines overlying the gravity contour near the Petermann rupture mark the steps of the contours at points P and P′.

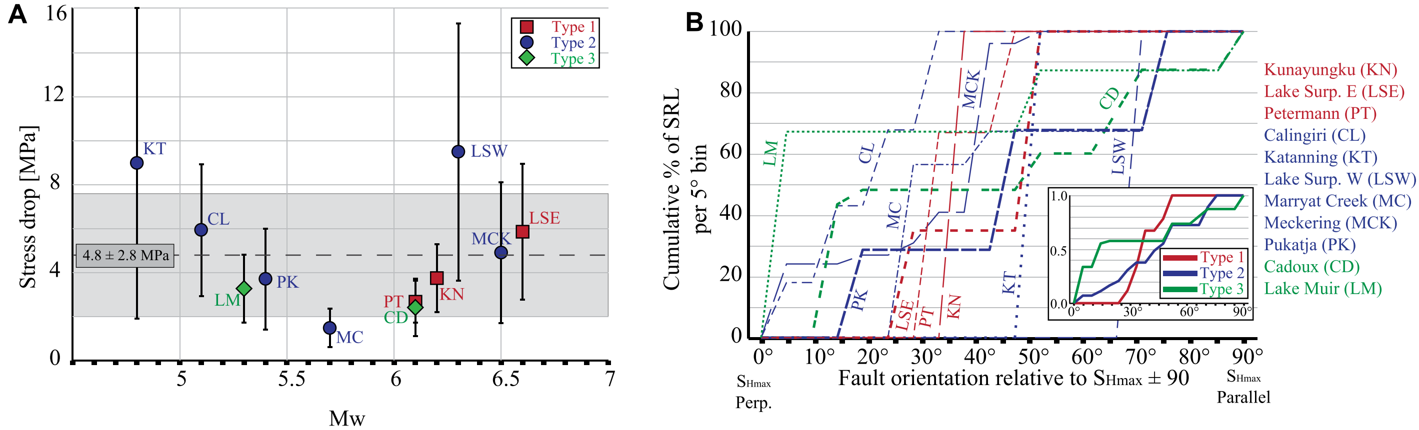

Figure 10. Relationship between stress drop and fault orientation for type 1, 2, and 3 events. (A) Stress drop relative to M_W with each event categorized into type. Uncertainties for each stress drop were calculated based on all stress drop estimates (Table S6 [see text footnote 1]). Dashed line and gray box indicate the average stress drop ± 1σ. (B) Cumulative percent of surface rupture length (*SLR*) relative to S_{Hmax} for each event, and per type (where 0° is S_{Hmax} perpendicular and 90° is S_{Hmax} parallel). Number of segments assigned to each rupture was taken from King et al. (2019) and is detailed in Tables S8–S10 and Figure S3 (see text footnote 1). While some type 2 and 3 events have well-aligned segments (i.e., perpendicular to S_{Hmax}), they generally have a larger range in orientations than type 1 events, which also have fewer segments.

ruptures are the Petermann, Kunayungku, and Lake Surprise East ruptures. These type 1 ruptures all share the following characteristics: (1) The host bedrock contains a dominant bedrock fabric (e.g., penetrative TMI fabric, surface geology foliations and faults) that is structurally continuous on the scale of surface ruptures (e.g., tens of kilometers) and oriented perpendicular-to-high-angle with respect to gravity gradients and S_{Hmax}; (2) the average surface rupture trace is oriented approximately parallel to this bedrock fabric; (3) surface rupture traces have the lowest range of S_{Hmax} values relative orientations (~28° to 52° from S_{Hmax} perpendicular; Fig. 10B and inset) and are all oriented approximately perpendicular to the gravity gradient; (4) mean $\Delta\sigma^{s}$ values derived from ensemble models are average (e.g., Lake Surprise East) to low (e.g., Petermann) relative to the average from all earthquakes (Fig. 10A); (5) observed *MD* is in the central third of the ruptures (Fig. 2); and (6) modeled displacement shapes are symmetric and lower amplitude, with a preference for elliptical shapes with centrally located, modeled *MD* (ellipse apices, Fig. 2) of similar value to *AD* (excluding Kunayungku).

The Petermann earthquake surface rupture is an example of a type 1 earthquake. The rupture orientation is relatively straight (Fig. 10B) and oriented between 27° and 47° (clockwise) from the normal of S_{Hmax} (Fig. 8). With a dip of ~30° (Attanayake et al., 2020), the fault is thus well oriented for reverse-oblique faulting. The rupture source can be generally described as a fault that is subparallel to micaceous foliations in the hosting bedrock. Parallelism with bedrock fabrics is suggested to have enhanced rupture gliding and promoted a low-stress-drop rupture (Attanayake et al., 2020). The modeled *MD* for triangular and elliptical shapes is similar to the *AD* (although the observed *MD* is ~7*AD*; Fig. 2). The critical behavior of the Petermann event observed in our probability distribution analysis of coseismic slip indicates that this event had a relatively weak fault strength, which resulted in a low-amplitude elliptical to *AD* slip distribution. The rupture trace is orthogonal to the regional gravity gradient (Fig. 9), and thus stress perturbations that could result from geological density contrasts could enhance the propensity toward reverse slip. The mean $\Delta\sigma^{s}$ derived from ensemble models of the Petermann earthquake (Table S1) is 2.7 ± 1.0 (1 σ) MPa; this is lower than the average $\Delta\sigma^{s}$ from all earthquakes and is low compared to median stress drops from intraplate earthquakes globally (~6 MPa; Allmann and Shearer, 2009).

Type 2

Type 2 crust contains multiple intersecting bedrock fabrics with varying orientations with respect to S_{Hmax} and gravity gradients, and no clearly dominant bedrock fabric at the scale of the individual rupture traces. Type 2 ruptures (Katanning, Calingiri, Lake Surprise West, Marryat Creek, Pukatja, Meckering) exhibit surface rupture complexity, as evidenced by a large range of orientations relative to the perpendicular of S_{Hmax} (0°–80°) and numerous stepped profiles in the cumulative *SRL* plot (Fig. 10B; Table S9 [see footnote 1]). Highly misoriented (i.e., all traces >45°–60° with respect to the perpendicular of S_{Hmax}) type 2 ruptures that are also influenced by surrounding high-angle structures (e.g., Lake Surprise West is bounded by Lake Surprise East and Kunayungku; Katanning is bounded by high-angle geophysical lineaments; Fig. 8) exhibit the highest mean $\Delta\sigma^{s}$ (Fig. 10A). Due to the high structural complexity of type 2 crust, type 2 ruptures exhibit the largest range in $\Delta\sigma^{s}$, including the lowest $\Delta\sigma^{s}$ event (Marryat Creek; Fig. 10A), and the greatest diversity in orientations with respect to S_{Hmax} (e.g., Calingiri vs. Lake Surprise West).

Type 3

Type 3 crust (locations of Lake Muir and Cadoux earthquakes) contains a dominant bedrock structure that is highly misaligned (i.e., <20°) to S_{Hmax} and thus is unfavorable for earthquake ruptures under the stress regime (see black arrows and dashed lineaments for Lake Muir and Cadoux in Fig. 8). Secondary structures include inherited faults and foliations that may be favorably or unfavorably oriented for brittle slip within the active stress field. Gravity gradients may be highly oblique to S_{Hmax} (Fig. 9). Surface rupture geometries may be highly complex and variably oriented, particularly the Cadoux earthquake (Figs. 1 and 10B); rupture traces tend to be more bimodally distributed into optimally (0°–10°; Fig. 10B) and highly misoriented (>60°; Fig. 10B) segments that reflect the interplay between extrinsic forcing by regional S_{Hmax} and the (misoriented) intrinsic structural properties of the host crust. This rupture type also exhibits the highest overall degree of asymmetry in both modeled and observed *MD*. The preferred rupture shape is triangular, which we attribute to an increased distribution of off-fault damage associated with rupture propagation through structurally unfavorable host rock. Both type 3 events considered here were shallow, with very large *SRL*:*W* ratios (Fig. 2) and relatively low $\Delta\sigma^{s}$ (Fig. 10A).

In terms of the Cadoux earthquake, the southern half of the surface rupture is primarily N-S oriented and well aligned with respect to S_{Hmax} for reverse faulting, while the northern half consists of a complex array of short E-W– and N-S–oriented rupture segments (Fig. 8). We posit that this change in structural complexity may primarily reflect two aspects: (1) increasing abundance of misoriented penetrative E-W–oriented structures to the north, which disrupted the N-S rupture and transferred slip across the complex fault array, and (2) increasing influence of a large-volume positive Bouguer anomaly to the north (indicated by circular contours in Fig. 9; also coincident with a zone of higher magnetic susceptibility on the TMI image in Fig. 8), which imparts a N-S gravity gradient that is approximately parallel to the average rupture trace orientation and is at a high angle to S_{Hmax}. We suggest that the latter effects locally increased the proportional contribution of the secondary horizontal stress (σ2) relative to the regional S_{Hmax} (σ1), thereby increasing the potential for rupture transfer onto higher-angle faults and overall rupture complexity. Local stress field rotations, including the possibility that the magnitude of the N-S–oriented compressive stress locally exceeds the regional S_{Hmax}, remain plausible hypotheses, collectively highlighting the potential for crustal structure to impart significant influence on rupture complexity. The slip asymmetry, with *MD* toward the rupture terminus (Fig. 2), poor statistical fit to all functions and highly variable slip tapers at either end of the rupture (Fig. 3), and abundant higher-frequency displacement energy with embedded triangular slip shapes (Figs. 2, 4, and 5) are additional characteristics of this rupture type.

DISCUSSION

High-Frequency Slip Maxima

The S-transform analysis reveals high-frequency ($k > 10$) signals in four events that are spatially coincident with high-spatial-slip gradients ($>10^{-3}$) at fault step-overs (Petermann), bends (Calingiri, Lake Surprise East) and fault intersections (Cadoux). Step-over widths on all faults were ubiquitously less than 2 km, consistent with empirical evidence for rupture propagation across <2-km-wide step-overs (Wesnousky, 2006, 2008).

For a type 1 ruptures like Petermann, we suggest the observed high slip gradients and high-frequency signals at the steps are related to highly dynamic stress concentrations associated with rupture propagation across neighboring fault segments (Elliott et al., 2009; Oglesby, 2008). The threshold value of spatial slip gradient that permits rupture jump over gaps and step-overs was previously suggested to be $>2 \times 10^{-4}$, which was based on the analysis of continental strike-slip earthquakes (Elliott et al., 2009). The observed spatial slip gradient in the Australian examples studied here is about one order of magnitude higher than the threshold value.

We note that the high slip gradient is only one aspect of the high-frequency signals; abrupt increases and decreases of slip within several hundred meters are also observed. These short-wavelength features are not predicted in the high-stress-concentration model (Elliott et al., 2009; Oglesby, 2008) nor the theory of shallowly connected faults (Oglesby, 2020). They may relate to short-wavelength geological anomalies with lower shear modulus relating to lithologies that are cut by the fault (Bürgmann et al., 1994) or shallowly connected fault segments (e.g., en-echelon fracture networks) only hundreds of meters long (Oglesby, 2020; Quigley et al., 2012). However, we did not find any evidence of lower-shear-modulus materials or short fault segments for these ruptures, based on examinations of geological and rupture maps, except for Cadoux (see next).

Zones of geometrically complicated interacting faults connected by opening fractures have been found elsewhere to produce the comparable high-frequency signal features to those observed here (e.g., see fig. 9 in Bürgmann et al., 1994). The linking fractures are able to transfer slip efficiently (Bürgmann et al., 1994). Fractures connecting fault bends and intersections were identified at Cadoux and Calingiri (Gordon and Lewis, 1980; Lewis et al., 1981). The high-frequency signal at Marryat Creek is correlated to the fault junction zone, where intersecting faults are orthogonally oriented with a wedge-shaped rupture geometry that can be considered kinematically and geometrically compatible. The mechanics of fault junctions suggests that the intersections of these types of faults could act as earthquake nucleation points and foci of maximum slip (Andrews, 1989). If fault steps, bends, or high-angle fault intersections act as kinematic asperities, we might anticipate these to coincide with slip maxima associated with maximum seismic energy release, and also high-frequency variations in slip as variations in the intrinsic characteristics of the fault zone influence the dynamics of the propagating rupture.

Slip Taper and Barriers

Here, we focus on the four events with slip taper $>10^{-3}$ that are considered outliers in Figure 3D. The high rupture tip taper value has been attributed elsewhere to (1) off-fault barriers of high frictional strength, (2) blocks of reduced shear modulus, (3) obliquely oriented structures, and (4) rupturing into a fault region that has previously experienced a large earthquake and is at a residual stress state (Cappa et al., 2014; Manighetti et al., 2004; Perrin et al., 2016; Scholz and Lawler, 2004). The faults in Australian cratonic regions are considered immature or incipient faults (following definitions from Brodsky et al., 2011; Perrin et al., 2016). An absence of scarps in proximity to these historic ruptures suggests that (4) it is unlikely to account for the observed displacement patterns (Clark et al., 2020; Clark and McCue, 2003; Crone et al., 2003).

In this section, detailed structures are described for each surface-rupturing earthquake. The Calingiri event is asymmetric in slip distribution with a high rupture tip taper (1.2×10^{-3}) at the southern tip (Fig. 3D; left end in Fig. 2). The southern tip was found to terminate at a nearly N-S–striking lineament of a low magnetic anomaly (dashed purple line in Fig. 8), while the whole rupture extends into a high-anomaly body, which sits on the hanging wall (Fig. 8).

The Pukatja event is 1.6 km long and has an asymmetric slip distribution with a high rupture tip taper value (2.9×10^{-3}) at the eastern tip (Fig. 3D; right end in Fig. 2). The eastern tip stops at a lineament of high magnetic susceptibility, while the other end (west) cuts into a body of relatively lower susceptibility (dash purple line in Fig. 8). The ends of other rupture tips of normal taper values (Fig. 3D) are not found to stop coincident with lineaments like those cases of high rupture tip taper values (Fig. 8).

The relatively high rupture tip taper in the right end (east) of Lake Surprise West and the left end (west) of Lake Surprise East (Fig. 3D) may be explained by the abrupt change of the dip direction of the hosting reverse fault (Fig. 1C; Bowman, 1992; Mohammadi et al., 2019). The Lake Surprise West event ruptured a NE-dipping fault, while the Lake Surprise East event ruptured a SW-dipping fault (Figs. 1B and 1C; Bowman, 1992). For the high rupture tip taper of the right tip (east) of the Lake Surprise East event, referring to the 1:250,000 Tennant Creek interpreted basement geology map (Johnston and Donnellan, 2001), we find that it stops at a location coincident with a fault separating volcaniclastic units from the undifferentiated granite (Fig. 1C).

These observations collectively suggest that obliquely orientated bedrock structures, identifiable as magnetic lineaments in geophysical data, coincide with the termini of some of the ruptures studied here and are associated with anonymously steep rupture tip tapers. No clear relationship is observed between tip taper steepness and prevailing rupture directivity, as proxied from estimates of epicentral location (Fig. 2). The relationship between high rupture tip taper value and the presence of magnetic lineaments at high angles to the rupture plane provides evidence that obliquely oriented bedrock structures may be effective barriers to rupture propagation. Lineaments orientated unfavorably to the rupture propagation direction may channel the propagating rupture into less efficient fracture pathways, therein dissipating fracture energy and terminating rupture propagation.

Through the study of structural control on rupture tip taper and the complexity of rupture segmentation, the role of preexisting structures in facilitating or stopping rupture development is evident. The concept of rupture potential may provide some hint to the relations between earthquake initiation point and terminus point (Weng and Ampuero, 2019). The rupture potential theory suggests that final rupture termini are located at places having the same rupture potential as that at the initiating position. The rupture potential theory determines the potential size of an earthquake provided that the spatial distribution of G_c/G_0 is obtained, where G_c and G_0 are the fracture energy and the steady-state energy release rate, respectively. The fracture energy is a function of rupture acceleration, which is not available before the earthquake occurs, and may be obtained from some physical scaling, thus introducing large uncertainties.

Applying this theory to the Australian cratonic earthquakes, we find that where an initiating point is in the intersecting part of two faults, which had a high rupture potential, the earthquake would rupture through other intersecting segments. This forms the complex rupture patterns as seen for the Meckering, Lake Muir, and Marryat Creek events. If the event initiated between two lineaments (dashed purple lines in Fig. 8) and was of lower rupture potential than that of the intersection points, the final rupture would be limited by two lineaments. This forms relatively simple rupture patterns, like the Pukatja and Katanning events, where ruptures were located between two large magnetic lineaments (dashed purple lines in Fig. 8). Therefore, the potential rupture length of a weak zone that is normal to the S_{Hmax} is controlled by two intersecting segments and is determined by the rupture potential of the initiating point.

In addition, the geophysical heterogeneity derived from the gravity map may reveal controlling factors on the Petermann earthquake, where no intersecting structure was detected through the TMI map. The gravity contours (marked by thick red lines in Fig. 9) to the NE of the surface rupture of the Petermann event demonstrate a sudden offset (at the positions P and P′ in Fig. 9) from the general trend where they are coincident with the location of the rupture, which is dipping to the NE. This sudden change of gravity contours reflects a shallow high-density anomaly beneath the surface (Fig. 9). The size of this anomaly is comparable to the surface rupture length and may have controlled the length of the final rupture.

Scaling between *MD*, *SRL*, and *Mw*

Figure 6 demonstrates that Australian cratonic earthquakes have larger *MD* and longer *SRL* than other earthquakes of comparable M_w (Wells and Coppersmith, 1994), with a few exceptions (e.g., Pukatja, Tennant Creek earthquakes in *SRL*). The Australian earthquakes also dominate the subset of the global data with hypocenters shallower than 7 km depth (filled symbols). We note that the small sample size limits our confidence in whether the earthquakes studied here represent the expected range of surface-rupturing earthquake behaviors in cold and stable cratonic crust, and we cannot dismiss possible effects of sampling bias. Nonetheless, we suggest that the shallowness of Australian cratonic earthquakes, and their potential for lateral rupture propagation at shallow depths through highly fractured cratonic crust, is expected to favor generation of higher *SRL:W* ratios and larger *MD* when compared to deeper, but otherwise similarly sized, crustal earthquakes in the global data sets (e.g., Wells and Coppersmith, 1994). High *SRL:W* ratios are commonly observed in large earthquakes ($Mw > 7$; Weng and Ampuero, 2019) where the rupture width is limited by regional brittle layer thickness. However, the shallowness and small rupture dimensions of the Australian cratonic earthquakes studied here preclude the involvement of ductile processes that limit the base of the rupture zone, such as enhanced viscous friction (e.g., Schueller et al., 2005).

The Kunayungku, Lake Surprise East, and Petermann earthquakes (type 1; Fig. 10) have simple surface rupture geometries with few definable segments or trend deviations (Fig. S3; Table S10 [see footnote 1]) but widely variable $\Delta\sigma^s$ (Fig. 10A; Table S6). We attribute this difference to the depth of the earthquake source. Our rupture width estimates for the Kunayungku and Lake Surprise East earthquakes range from 9.8 to 11.6 km (Table S5), while published estimates extend from the surface to depths of >6 km (Choy and Bowman, 1990) and up to 10–16 km (Bowman, 1991; Mohammadi et al., 2019). InSAR inversion, CMT modeling, and seismological analyses suggest the Petermann earthquake was limited to the top ~4 km of the crust (Attanayake et al., 2020; Hejrani and Tkalčić, 2019; Polcari et al., 2018). The frictional strength of fault rocks in the shallow crust (<5 km) in cratonic areas is proposed to be much lower than deeper equivalents (Bamford, 1976; Denham et al., 1980), and thus otherwise equivalent ruptures channeled along highly anisotropic crustal weak zones (type 1) that extend to greater depths are hypothesized to have larger $\Delta\sigma^s$ (Fig. 10).

We further speculate that increasing cratonic crustal strength with depth may inhibit downward rupture propagation via increasing fault friction and decreasing fracture continuity, while imposing a discernible effect on spectra of coseismic slip distributions (Fig. 5B). For many earthquakes (e.g., Calingiri, Petermann), we found high-energy concentrations at short wavelengths (1–5 km; Fig. 5) that are comparable with rupture widths. We envisage the rupture process to involve progressive energy bursts of propagating fractures with dimensions (e.g., diameters) set by the downdip rupture width; these fractures coalesce to impart higher-frequency displacement variations that are manifested as embedded shapes within the gross rupture profiles. These signals would be more discernible in shallower earthquakes and more attenuated in deeper earthquakes with smaller *SRL:W* ratios (e.g., Pukatja, Lake Surprise West).

This hypothesis is not incompatible with the large range of stress drops and rupture displacement shapes we observed in the shallow cratonic earthquakes, because aspects such as coseismic slip and rupture length could be highly dependent on shallow (<5 km) variations in crustal structure, lithology, and other factors while still adhering to our hypothesis of depth-limited behavior. The rupture of depth-limited shallow earthquakes may be comparably less constrained from propagating laterally due to the presence of lithologic and structural heterogeneities that could enhance coseismic rupture growth (Attanayake et al., 2020). Just as the lateral dimension of fault step-overs is important in limiting the size and mechanics of laterally propagating ruptures (Wesnousky, 2006), perhaps variations in the strength (e.g., Mooney et al., 2012) and stress distributions in cratonic crust favor depth partitioning of earthquakes with limited rupture widths. Our hypothesis also does not preclude the occurrence of deep cratonic earthquakes, such as the 1989 magnitude 5.6 Uluru earthquake (hypocenter depth = 31 km; Michael-Leiba et al., 1994). Rather, we suggest that the strength and strongly segmented nature of fractures in cratonic lithosphere could suppress upward propagation of deep earthquakes and downward propagation of shallow earthquakes, and thereby potentially limit earthquake maximum M_w in cratons (e.g., Mooney et al., 2012).

Implications for Seismic Hazard: Inputs

The principal aim of probabilistic fault displacement hazard analysis (PFDHA) is to evaluate the potential for ground surface displacements of varying amounts, and across varying time scales, associated with seismogenic fault rupture (Moss and Ross, 2011; Youngs et al., 2003). Empirical distributions for *SRL*, *MD*, *AD*, spatial variability of slip, and other statistical parameters are essential inputs into PFDHA calculations, which include probabilities of surface rupture at different *Mw* and slip exceedance distributions (Moss and Ross, 2011).

Figure 11A presents a new surface rupture probability curve for Australian cratonic earthquakes and compares this curve to prior curves from global regressions (Moss and Ross, 2011). Australian earthquake data were obtained for the period 1 January 1900 to 21 October 2020 from Geoscience Australia's Earthquake Catalogue (https://earthquakes.ga.gov.au/). We note that this earthquake catalogue does not include the revised M_W estimates from the 2018 National Seismic Hazard Assessment (NSHA18; Allen et al., 2018), from which our surface rupture M_W values were sourced. However, the NSHA18 catalogue only extends to 2017 and excludes the Lake Muir earthquake. The earthquake catalogue was restricted to onshore Precambrian nonextended crust only (Fig. 1). We applied magnitude completeness cutoffs based on the Australian continent M_C estimates of Allen et al. (2018): M_C 6.5 > 1920; M_C 6.0 > 1920; M_C 4.5 > 1960; M_C 4.0 > 1970.

The percent of all earthquakes in each 0.1 M_w increment that caused surface rupture was used as point data and fit by a regression curve with the logistic function following the method of Moss and Ross (2011). Six of nine Australian stable continental region earthquakes in this period with $M_w \geq 6.0$ generated surface ruptures, and thus the probability of surface rupture increases steeply over the $6.0 \leq M_w \leq 6.5$ interval. Termination of the Australian stable continental region probability curve below 1.0 and at values of $M_w > 6.6$ was intended to reflect epistemic uncertainty pertaining to the short historical seismologic record. Given the diverse nature of the reverse fault and Australian stable continental region curves, PFDHA could consider implementation of a logic tree weighted approach amongst these functions, depending upon the geological-seismological inputs and the desired conservativity of the analysis. As many deeper earthquakes in areas of enhanced sedimentary thickness contribute to the global regression, we favor weighting toward the stable continental region Oz curve (0.6–0.7) in Australian bedrock terrains.

Figure 11B compares observed *AD* and *MD* for the Australian earthquakes against modeled *AD* and *MD* derived from regressions in the preeminent PFDHA framework used to evaluate

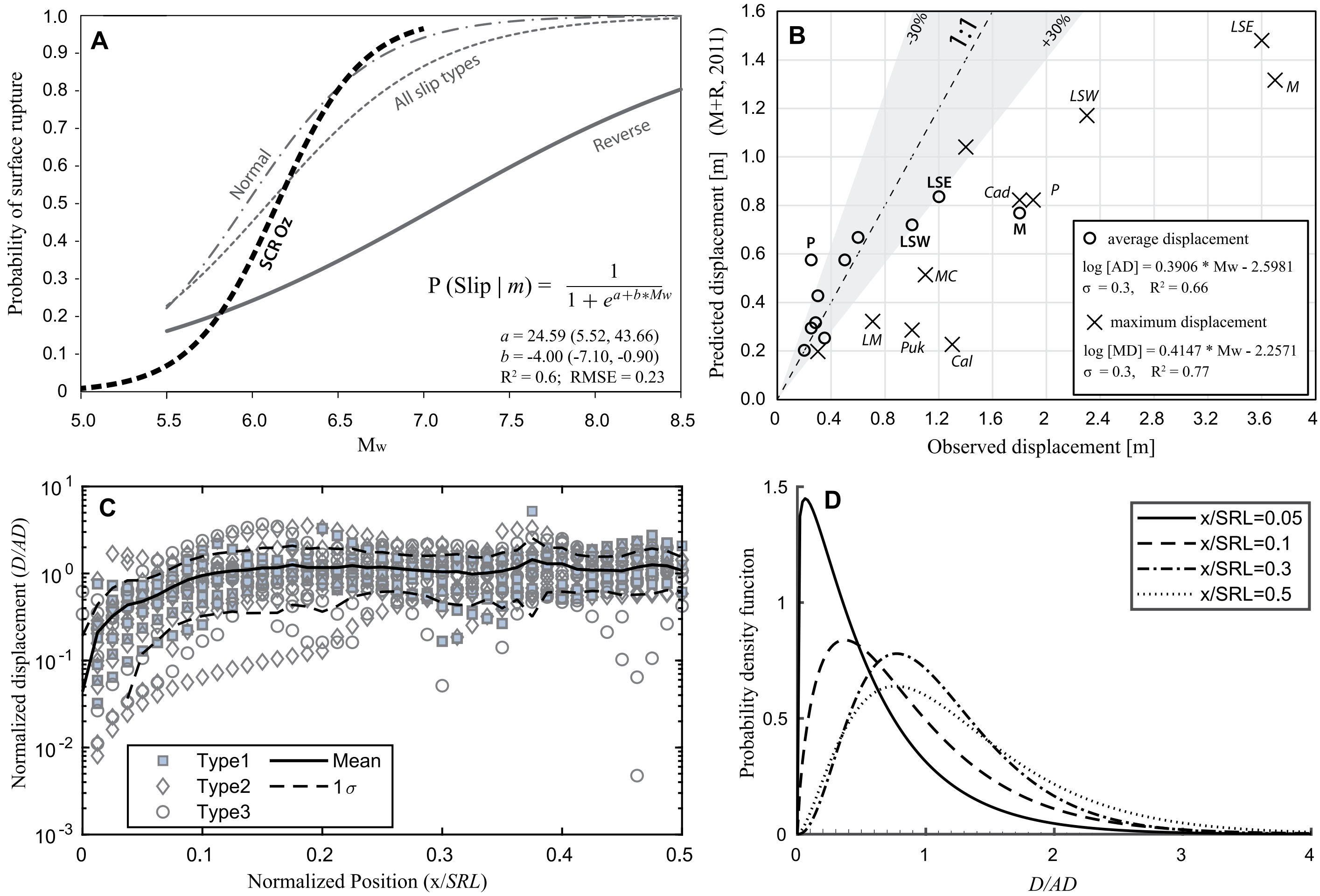

Figure 11. (A) Probability of surface rupture for reverse faults (from Moss and Ross, 2011), normal faults (from Youngs et al., 2003), all slip kinematic types (from Youngs et al., 2003), and Australian stable continental region earthquakes (SCR Oz; this study). Empirical distributions were fit using logistic regressions; the SCR Oz curve is a best fit to a two-period moving average. The probability for all reverse-faulting events is significantly lower than that of normal and all slip types for equivalent M_w; however, the SCR Oz probability is significantly higher for equivalent M_w. Reverse, normal, and all distributions are only valid in the range of $5.5 \leq M_w \leq 8.0$, and SCR Oz is valid only for $4.0 \leq M_w \leq 6.6$. RMSE—root mean square error. (B) Predicted values for average (*AD*) and maximum (*MD*) surface rupture displacements from the equations of Moss and Ross (2011) plotted against the observed *AD* and *MD* values from King et al. (2019) and this study. The Moss and Ross (2011) equations are: Log(*AD*) = 0.3244 × Mw – 2.2192 and Log(*MD*) = 0.5102 × Mw – 3.1971. The 1:1 line is flanked by ±30% error bounds. Outlier data points are labeled in bold (*AD*) and italics (*MD*): P—Petermann, LSE—Lake Surprise East, LSW—Lake Surprise West, M—Meckering, LM—Lake Muir, Puk—Pukatja, Cal—Calingiri. New M_w-based regression fits for *AD* and *MD* based only on the Australian stable continental region data appear in the legend; given that 9 of 11 Australian earthquakes have observed *MD* >> modeled (Moss and Ross, 2011) *MD*, these new regressions may be preferred for stable continental region probabilistic fault displacement hazard analysis (PFDHA) analyses. (C) Normalized displacement (discrete displacement/*AD*) for Australian stable continental region earthquakes plotted as a function of rupture half length (*x/L*, where *x/L* = 0 is the rupture tip, and *x/L* = 0.5 is the rupture midpoint). *SLR*—surface rupture length. (D) Gamma distributions for spatial variability in *AD* at different normalized positions (most proximal to rupture tip, *x* = 0.05; rupture midpoint, *x* = 0.5). These distributions may be used to obtain an *AD* probability distribution for PFDHA at specific sites (e.g., Moss and Ross, 2011); intermediate positions along the fault will have intermediate profiles.

reverse faults (Moss and Ross, 2011; equations in Fig. 11 caption). Almost all Australian earthquakes have observed *AD* within ±30% of the predicted *AD* from Moss and Ross (2011), with the exception of the low-slip, low-stress-drop Petermann earthquake (P in Fig. 11). However, 9 of 11 Australian earthquakes have observed *MD* >> modeled *MD* (>+30% of predicted). We therefore calculated new *AD* and *MD* to M_w linear regressions and present these in Figure 11B. These formulae could be used or statistically preferred to other regressions (in a weighted logic tree content) for PFDHAs in stable continental region bedrock regions.

In terms of displacement profiles, 8 of 11 earthquakes (73%) have observed *MD* in the central third of the rupture (Fig. 2), and 7 of 11 earthquakes (64%) have "symmetric" best-fitting functions (Fig. 3C; Table S2). Although a flat-line fit (displacement at any given point along the rupture is equal to *AD*) is not the preferred shape for any event, it produces close results (i.e., *AD* ≈ modeled *MD*) to the best fit in the Petermann and Lake Surprise East events. Incremental displacements along a specified fault in a type 1 setting (Fig. 10) could thus be appropriately modeled using *AD* estimates obtained from the scaling relationship in Figure 11B. From the perspective of PFDHA, however, it is difficult to accurately forecast the shape and symmetry of surface rupture displacement fields for future earthquakes across a diverse range of stable continental region settings. To resolve this, we normalized incremental displacements (*D*) against *AD* at fault positions (*x*) against *SRL* for all rupture types. The *x* axis is the rupture half length, with each rupture yielding two data points for each displacement increment. We fit a mean regression and 1σ error bounds to all data (Fig. 11C).

Figure 11C shows *D* is $\leq$ *AD* within the first 10% of the *SRL* (measured from either rupture tip), and *D* is $\geq$ *AD* within the middle 80% of the rupture (0.2–0.5). The highest values of *D* (i.e., >*AD*) and lowest uncertainty bounds are observed in the middle quintile of the rupture. Type 2 and 3 faults exhibit the largest variability along the rupture trace (i.e., *D/AD* > 1σ bounds). The largest 1σ incremental *D/AD* values occur in the first 20% of the rupture length. PFDHA practitioners could consider the structural-geophysical setting type (Fig. 10) with these data (Fig. 11) to select conservative bounds for incremental PFDHA estimates depending upon the location of a site along a rupture trace. At the simplest level, the mean curve and 1σ bounds presented in Figure 11C could represent a reasonable approximation of *D/AD* irrespective of geological setting.

As a final demonstration of how the results of this study could inform PFDHA, we show gamma probability distribution functions (PDFs) for *D/AD* at fixed values of *x/SRL* ranging from the first 5% of the surface rupture (*x/SRL* = 0.05) to the rupture midpoint (*x/SRL* = 0.5). PDFs shift to higher proportionate values of *D/AD* toward the rupture midpoint (i.e., *D* > *AD*) but retain strong probability distributions of *D* < *AD* at all locations.

CONCLUSIONS

(1) In our data set of Australian stable continental region earthquakes, *AD:MD* ratios range from 0.13 (Petermann earthquake) to 0.67 (Katanning) with a mean of 0.36 ± 0.14 (1σ). Of the eight ruptures analyzed, 50% exhibit unilateral and 50% exhibit bilateral rupture directivity. If the observed and modeled positions of *MD* relative to *SRL* are combined, ~68% of earthquakes have *MD* in the middle third of the rupture, and 16% have *MD* in each of the end thirds.

(2) Surface coseismic slip distributions for the studied earthquakes generally adhers to asymmetric triangular or elliptical shapes, but there is not a preferred shape for all events studied here. There are two prevailing end-member forms of coseismic along-strike slip distribution: the low-curvature to rectangular shape (e.g., Petermann; close to an elliptical shape) for earthquakes with a roughly straight and localized damage zone (type 1 structures), and the higher-curvature shape (e.g., Meckering; close to a triangular shape) for earthquakes with complex segmented surface rupture geometries. The latter earthquakes are proposed to originate from higher frictional stress on the fault plane relative to the former and may include intensive off-fault damage zones. Crustal structure plays an important role in rupture characteristics.

(3) The S-transform analysis on the residuals suggests that while basic shapes may be representative of the slip distributions, there are significant contributions in the form of high-spatial-frequency (short-wavelength) signals that we attribute to factors that influence the rupture process, including stress concentrations coincident with fault geometric complexities (e.g., step-overs or intersections) and depth controls on the rupture source (e.g., shallow earthquakes exhibit high-frequency displacement variations with wavelengths similar to rupture width).

(4) The higher value of *MD* and *SRL* in Australia compared to global examples may be attributed to the shallow earthquake hypocenters in the former data set (mean 3.6 ± 1.9 km). Shallow earthquakes are expected to be more likely to have *SRL* ≈ subsurface rupture length, *AD* ≈ subsurface *AD*, and *MD* ≈ subsurface *MD*. Enhanced stress concentrations at geometrically compatible fault junctions (e.g., Marryat Creek) may further increase *MD*.

(5) Surface rupture geometries are controlled by bedrock fabrics, which are mainly revealed by the TMI map. Of the total combined (summative) length of all surface ruptures (~148 km), we estimate that between 133 km (90%) and 145 km (98%) lengths align with the geophysical structure in the host basement rocks. When the host bedrock contains a dominant bedrock fabric that is structurally continuous at the scale of surface ruptures (e.g., tens of kilometers) and oriented perpendicular-to-high angle with respect to gravity gradients and S_{Hmax}, then it tends to produce relatively simple and straight surface rupture (type 1; e.g., Petermann). If the bedrock fabric consists of intersected segments with variable orientations at the scale that is comparable to the surface rupture length, it tends to produce complex surface ruptures (type 2 and type 3; e.g., Meckering and Cadoux). At the scale of this study, we are unable to determine whether TMI fabric geometries truly parallel rupture geometries in three dimensions, or if they are simply aligned in trace; if only the latter is true, TMI fabrics may play more alternative roles in enhancing rupture propagation (e.g., fluid conduits) rather than simply providing zones of enhanced frictional weakness.

(6) New $\Delta\sigma^s$ estimates are derived based on published estimates and three methods incorporating *W*, M_O, *AD*, and μ. The average stress drop for all studied earthquakes as 4.8 ± 2.8 (1σ). The $\Delta\sigma^s$ values derive from ensemble models for the type 1 and type 3 earthquakes are close to or lower than the average from all earthquakes, and type 2 earthquakes show large variations in $\Delta\sigma^s$.

(7) The rupture tip taper value at the termini found in this study is consistent with the result from a global database and complements existing data in slip mode. The asymmetry of displacement distribution and extremely steep rupture tip tapers are found to be affected by bedrock fabrics obliquely oriented with respect to the rupture strike.

(8) The interaction among regional S_{Hmax}, intersecting segments, and the gravity gradient increases surface rupture complexity (e.g., the Cadoux event). The segment length of a magnetic lineament that is normal to S_{Hmax} may set the limit of an earthquake surface rupture by intersecting other lineaments at low angle (<45°) to the S_{Hmax}.

(9) *MD* values are commonly (8 of 11 earthquakes; 73%) located coincident with fault steps, bends, and/or high-angle fault intersections. S-transform analysis reveal that the spike-like high-frequency slip maxima also coincids with fault steps and junctions, suggesting concentrations of hierarchical fractal fault damage networks embedded within areas of geometric and kinematic incompatibility. The geometric compatibility or incompatibility of fault intersection zones provides a fruitful avenue for future research. It is clear from this study that fault intersections should not be simply treated as converging areas where displacement tapers to net-zero slip in seismic hazard. In some cases, fault geometric complexities could be forecasted to have slip maxima; this is particularly important to consider in probabilistic fault displacement seismic hazard analyses for critical infrastructure.

(10) The earthquakes in Australian stable continental regions have a higher surface rupture probability, at *Mw* > 5.7, than predicted from prior reverse-fault regression curves, necessitating consideration of additional surface rupture probability functions in PFDHA. Incremental surface displacements increase to approximately *AD* within the first 10% of the *SRL* (measured from either rupture tip), and *D* is $\geq$ *AD* within the middle 80% of the rupture.

ACKNOWLEDGMENTS

We would like to acknowledge the Noongar people of southwest Western Australia, the Warumungu people of Tennant Creek, and the Antakirinja, Yankunytjatjara, and Pitjantjatjara people of the Western Desert and Aṉangu Pitjantjatjara Yankunytjatjara (APY) lands in South Australia/Northern Territory, as the traditional custodians of the land on which all historic surface ruptures occurred, and where the data described in this paper were collected. This research was funded by the Australian Research Council through Discovery Grant DP170103350 to M. Quigley. We acknowledge the contributions of Dan Clark and Trevor Allen from Geoscience Australia toward enhancing our knowledge of Australian earthquakes. T. King received support from the David Hay Postgraduate Writing-Up Award (University of Melbourne). H. Yang received the Melbourne Research Scholarship, the Baragwanath Travel Scholarship, and the Albert Shimmins Writing-Up Award from the University of Melbourne to assist in research development. Geophysical maps were produced using the Generic Mapping Tools (GMT) package (Wessel et al., 2013).

REFERENCES CITED

Adams, J., Wetmiller, R.J., Hasegawa, H.S., and Drysdale, J., 1991, The first surface faulting from a historical intraplate earthquake in North America: Nature, v. 352, no. 6336, p. 617–619, https://doi.org/10.1038/352617a0.

Allen, T., Leonard, M., Ghasemi, H., and Gibson, G., 2018, The 2018 National Seismic Hazard Assessment: Earthquake Epicentre Catalogue: Canberra, ACT, Australia, Geoscience Australia (GA), Commonwealth of Australia, GA Record 2018/30, 52 p.

Allmann, B.P., and Shearer, P.M., 2009, Global variations of stress drop for moderate to large earthquakes: Journal of Geophysical Research–Solid Earth, v. 114, no. B1, B01310, https://doi.org/10.1029/2008JB005821.

Andrews, D.J., 1989, Mechanics of fault junctions: Journal of Geophysical Research–Solid Earth and Planets, v. 94, no. B7, p. 9389–9397, https://doi.org/10.1029/JB094iB07p09389.

Attanayake, J., King, T.R., Quigley, M.C., Gibson, G., Clark, D., Jones, A.G., Brennand, S.L., and Sandiford, M., 2020, Rupture characteristics and bedrock structural control of the 2016 M w 6.0 intraplate earthquake in the Petermann Ranges, Australia: Bulletin of the Seismological Society of America, v. 110, no. 3, p. 1037–1045, https://doi.org/10.1785/0120190266.

Bamford, W.E., 1976, Evolution of stresses in rock masses, as related to compressive strengths and plate tectonics, *in* Investigation of Stress in Rock: Advances in Stress Measurement Symposium (Sydney): Barton, ACT, Australia, Institution of Engineers, no. 76/4, p. 63–70.

Bowman, J.R., 1991, Geodetic evidence for conjugate faulting during the 1988 Tennant Creek, Australia, earthquake sequence: Geophysical Journal International, v. 107, no. 1, p. 47–56, https://doi.org/10.1111/j.1365-246X.1991.tb01155.x.

Bowman, J.R., 1992, The 1988 Tennant Creek, Northern Territory, earthquakes—A synthesis: Australian Journal of Earth Sciences, v. 39, no. 5, p. 651–669, https://doi.org/10.1080/08120099208728056.

Brodsky, E.E., Gilchrist, J.J., Sagy, A., and Collettini, C., 2011, Faults smooth gradually as a function of slip: Earth and Planetary Science Letters, v. 302, no. 1–2, p. 185–193, https://doi.org/10.1016/j.epsl.2010.12.010.

Brown, S.R., and Scholz, C.H., 1985, Broad bandwidth study of the topography of natural rock surfaces: Journal of Geophysical Research–Solid Earth and Planets, v. 90, no. B14, p. 12575–12582, https://doi.org/10.1029/JB090iB14p12575.

Bürgmann, R., Pollard, D.D., and Martel, S.J., 1994, Slip distributions on faults: Effects of stress gradients, inelastic deformation, heterogeneous host-rock stiffness, and fault interaction: Journal of Structural Geology, v. 16, no. 12, p. 1675–1690, https://doi.org/10.1016/0191-8141(94)90134-1.

Cappa, F., Perrin, C., Manighetti, I., and Delor, E., 2014, Off-fault long-term damage: A condition to account for generic, triangular earthquake slip profiles: Geochemistry Geophysics Geosystems, v. 15, no. 4, p. 1476–1493, https://doi.org/10.1002/2013GC005182.

Choy, G.L., and Bowman, J.R., 1990, Rupture process of a multiple main shock sequence: Analysis of teleseismic, local, and field observations of the Tennant Creek, Australia, earthquakes of January 22, 1988: Journal of Geophysical Research–Solid Earth, v. 95, no. B5, p. 6867–6882, https://doi.org/10.1029/JB095iB05p06867.

Clark, D., 2012, Neotectonic Features Database: Geoscience Australia, Commonwealth of Australia: https://doi.org/http://pid.geoscience.gov.au/dataset/ga/74056.

Clark, D., and McCue, K., 2003, Australian paleoseismology: Towards a better basis for seismic hazard estimation: Annals of Geophysics, v. 46, no. 5, p. 1087–1105, https://doi.org/10.4401/ag-3447.

Clark, D., McPherson, A., and Van Dissen, R., 2012, Long-term behaviour of Australian stable continental region (SCR) faults: Tectonophysics, v. 566, p. 1–30, https://doi.org/10.1016/j.tecto.2012.07.004.

Clark, D., McPherson, A., Allen, T., and De Kool, M., 2014, Coseismic surface deformation caused by the 23 March 2012 M-w 5.4 Ernabella (Pukatja) earthquake, Central Australia: Implications for fault scaling relations in cratonic settings: Bulletin of the Seismological Society of America, v. 104, no. 1, p. 24–39, https://doi.org/10.1785/0120120361.

Clark, D., Brennand, S., Brenn, G., Garthwaite, M.C., Dimech, J., Allen, T.I., and Standen, S., 2020, Surface deformation relating to the 2018 Lake Muir earthquake sequence, southwest Western Australia: New insight into stable continental region earthquakes: Solid Earth, v. 11, no. 2, p. 691–717, https://doi.org/10.5194/se-11-691-2020.

Cowie, P.A., and Scholz, C.H., 1992a, Growth of faults by accumulation of seismic slip: Journal of Geophysical Research–Solid Earth, v. 97, no. B7, p. 11085–11095, https://doi.org/10.1029/92JB00586.

Cowie, P.A., and Scholz, C.H., 1992b, Physical explanation for the displacement length relationship of faults using a post-yield fracture-mechanics model: Journal of Structural Geology, v. 14, no. 10, p. 1133–1148, https://doi.org/10.1016/0191-8141(92)90065-5.

Crone, A.J., Machette, M.N., and Bowman, J.R., 1992, Geologic Investigations of the 1988 Tennant Creek, Australia, Earthquakes - Implications for Paleoseismicity in the Stable Continental Regions (U.S. Geological Survey Bulletin 2032-A): U.S. Geological Survey, https://doi.org/https://doi.org/10.3133/b2032A.

Crone, A.J., De Martini, P.M., Machette, M.N., Okumura, K., and Prescott, J.R., 2003, Paleoseismicity of two historically quiescent faults in Australia: Implications for fault behavior in stable continental regions: Bulletin of the Seismological Society of America, v. 93, no. 5, p. 1913–1934, https://doi.org/10.1785/0120000094.

Dawson, J., Cummins, P., Tregoning, P., and Leonard, M., 2008, Shallow intraplate earthquakes in Western Australia observed by interferometric synthetic aperture radar: Journal of Geophysical Research–Solid Earth, v. 113, no. B11, B11408, https://doi.org/10.1029/2008JB005807.

Denham, D., 1988, Australian seismicity—The puzzle of the not so stable continent: Seismological Research Letters, v. 59, no. 4, p. 235–240, https://doi.org/10.1785/gssrl.59.4.235.

Denham, D., Alexander, L.G., and Worotnicki, G., 1980, The stress field near the sites of the Meckering (1968) and Calingiri (1970) earthquakes, Western Australia: Tectonophysics, v. 67, no. 3–4, p. 283–317, https://doi.org/10.1016/0040-1951(80)90271-1.

Denham, D., Alexander, L.G., Everingham, I.B., Gregson, P.J., Mccaffrey, R., and Enever, J.R., 1987, The 1979 Cadoux earthquake and intraplate stress in Western Australia: Australian Journal of Earth Sciences, v. 34, no. 4, p. 507–521, https://doi.org/10.1080/08120098708729429.

Dentith, M.C., Dent, V.F., and Drummond, B.J., 2000, Deep crustal structure in the southwestern Yilgarn craton, Western Australia: Tectonophysics, v. 325, no. 3–4, p. 227–255, https://doi.org/10.1016/S0040-1951(00)00119-0.

Dentith, M., Clark, D., and Featherstone, W., 2009, Aeromagnetic mapping of Precambrian geological structures that controlled the 1968 Meckering earthquake (Ms 6.8): Implications for intraplate seismicity in Western Australia: Tectonophysics, v. 475, no. 3–4, p. 544–553, https://doi.org/10.1016/j.tecto.2009.07.001.

Dolan, J.F., and Haravitch, B.D., 2014, How well do surface slip measurements track slip at depth in large strike-slip earthquakes? The importance of fault structural maturity in controlling on-fault slip versus off-fault surface deformation: Earth and Planetary Science Letters, v. 388, p. 38–47, https://doi.org/10.1016/j.epsl.2013.11.043.

Elliott, A.J., Dolan, J.F., and Oglesby, D.D., 2009, Evidence from coseismic slip gradients for dynamic control on rupture propagation and arrest through stepovers: Journal of Geophysical Research–Solid Earth, v. 114, no. B2, B02313, https://doi.org/10.1029/2008JB005969.

Frankel, A., 1991, High-frequency spectral falloff of earthquakes, fractal dimension of complex rupture, b value, and the scaling of strength on faults: Journal of Geophysical Research–Solid Earth, v. 96, no. B4, p. 6291–6302, https://doi.org/10.1029/91JB00237.

Gabrielov, A., Keilis-Borok, V., and Jackson, D.D., 1996, Geometric incompatibility in a fault system: Proceedings of the National Academy of Sciences of the United States of America, v. 93, no. 9, p. 3838–3842, https://doi.org/10.1073/pnas.93.9.3838.

Gold, R.D., Reitman, N.G., Briggs, R.W., Barnhart, W.D., Hayes, G.P., and Wilson, E., 2015, On- and off-fault deformation associated with the September 2013 Mw 7.7 Balochistan earthquake: Implications for geologic slip rate measurements: Tectonophysics, v. 660, p. 65–78, https://doi.org/10.1016/j.tecto.2015.08.019.

Gordon, F.R., and Lewis, J.D., 1980, The Meckering and Calingiri Earthquakes October 1968 and March 1970: Meckering, Western Australia, Geological Survey of Western Australia, 228 p.

Griffith, W.A., Di Toro, G., Pennacchioni, G., Pollard, D.D., and Nielsen, S., 2009, Static stress drop associated with brittle slip events on exhumed faults: Journal of Geophysical Research–Solid Earth, v. 114, no. B2, B02402, https://doi.org/10.1029/2008JB005879.

Haeussler, P.J., Schwartz, D.P., Dawson, T.E., Stenner, H.D., Lienkaemper, J.J., Sherrod, B., Cinti, F.R., Montone, P., Craw, P.A., Crone, A.J., and Personius, S.F., 2004, Surface rupture and slip distribution of the Denali and Totschunda faults in the 3 November 2002 M 7.9 earthquake, Alaska: Bulletin of the Seismological Society of America, v. 94, no. 6, p. S23–S52, https://doi.org/10.1785/0120040626.

Hejrani, B., and Tkalčić, H., 2019, The 20 May 2016 Petermann Ranges earthquake: Centroid location, magnitude and focal mechanism from full waveform modelling: Australian Journal of Earth Sciences, v. 66, no. 1, p. 37–45, https://doi.org/10.1080/08120099.2018.1525783.

Huang, Y., Ellsworth, W.L., and Beroza, G.C., 2017, Stress drops of induced and tectonic earthquakes in the central United States are indistinguishable: Science Advances, v. 3, no. 8, e1700772, https://doi.org/10.1126/sciadv.1700772.

Johnston, A., and Donnellan, N., 2001, Tennant Creek 1:250,000 Integrated Interpretation of Geophysics and Mapped Geology: Alice Springs, Australia, Northern Territory Geological Survey, scale 1:250,000.

Johnston, A.C., 1989, The seismicity of 'stable continental interiors,' *in* Gregersen, S., and Basham, P.W., eds., Earthquakes at North-Atlantic Passive Margins: Neotectonics and Postglacial Rebound: Dordrecht, Netherlands, Springer, NATO Advanced Study Institute (ASI) Series C: Mathematical and Physical Sciences Volume 266, p. 299–327, https://doi.org/10.1007/978-94-009-2311-9_18.

Kaneko, Y., and Fialko, Y., 2011, Shallow slip deficit due to large strike-slip earthquakes in dynamic rupture simulations with elasto-plastic off-fault response: Geophysical Journal International, v. 186, no. 3, p. 1389–1403, https://doi.org/10.1111/j.1365-246X.2011.05117.x.

King, G., 1983, The accommodation of large strains in the upper lithosphere of the Earth and other solids by

self-similar fault systems—The geometrical origin of b-value: Pure and Applied Geophysics, v. 121, no. 5–6, p. 761–815, https://doi.org/10.1007/BF02590182.
King, T.R., Quigley, M.C., and Clark, D., 2018, Earthquake environmental effects produced by the Mw 6.1, 20th May 2016 Petermann earthquake, Australia: Tectonophysics, v. 747, p. 357–372, https://doi.org/10.1016/j.tecto.2018.10.010.
King, T.R., Quigley, M., and Clark, D., 2019, Surface-rupturing historical earthquakes in Australia and their environmental effects: New insights from re-analyses of observational data: Geosciences, v. 9, no. 10, p. 408, https://doi.org/10.3390/geosciences9100408.
Klinger, Y., 2010, Relation between continental strike-slip earthquake segmentation and thickness of the crust: Journal of Geophysical Research–Solid Earth, v. 115, no. B7, B07306, https://doi.org/10.1029/2009JB006550.
Leonard, M., 2008, One hundred years of earthquake recording in Australia: Bulletin of the Seismological Society of America, v. 98, no. 3, p. 1458–1470, https://doi.org/10.1785/0120050193.
Leonard, M., 2010, Earthquake fault scaling: Self-consistent relating of rupture length, width, average displacement, and moment release: Bulletin of the Seismological Society of America, v. 100, no. 5a, p. 1971–1988, https://doi.org/10.1785/0120090189.
Leonard, M., Burbidge, D., Allen, T., Robinson, D., McPherson, A., Clark, D., and Collins, C., 2014, The challenges of probabilistic seismic-hazard assessment in stable continental interiors: An Australian example: Bulletin of the Seismological Society of America, v. 104, no. 6, p. 3008–3028, https://doi.org/10.1785/0120130248.
Lewis, J.D., Daetwyler, N.A., Bunting, J.A., and Moncrieff, J.S., 1981, The Cadoux Earthquake, Western Australia: Geological Survey of Western Australia Report 11, 133 p.
Madariaga, R., 1977, Implications of stress-drop models of earthquakes for the inversion of stress drop from seismic observations, *in* Wyss, M., ed., Stress in the Earth; Contributions to Current Research in Geophysics (CCRG): Basel, Switzerland, Birkhäuser Verlag, p. 301–316, https://doi.org/10.1007/978-3-0348-5745-1_19.
Mai, P.M., and Beroza, G.C., 2002, A spatial random field model to characterize complexity in earthquake slip: Journal of Geophysical Research-Solid Earth, v. 107, no. B11, p. ESE10-11–ESE10-21, https://doi.org/10.1029/2001JB000588.
Manighetti, I., King, G., and Sammis, C.G., 2004, The role of off-fault damage in the evolution of normal faults: Earth and Planetary Science Letters, v. 217, no. 3–4, p. 399–408, https://doi.org/10.1016/S0012-821X(03)00601-0.
Manighetti, I., Zigone, D., Campillo, M., and Cotton, F., 2009, Self-similarity of the largest-scale segmentation of faults: Implications for earthquake behavior: Earth and Planetary Science Letters, v. 288, no. 3–4, p. 370–381, https://doi.org/10.1016/j.epsl.2009.09.040.
McCue, K., Barlow, B.C., Denham, D., Jones, T., Gibson, G., and Michael-Leiba, M., 1987, Another chip off the old Australian block: Eos (Washington, D.C.), v. 68, no. 26, p. 609–612, https://doi.org/10.1029/EO068i026p00609.
McGill, S.F., and Rubin, C.M., 1999, Surficial slip distribution on the central Emerson fault during the June 28, 1992, Landers earthquake, California: Journal of Geophysical Research–Solid Earth, v. 104, no. B3, p. 4811–4833, https://doi.org/10.1029/98JB01556.
Michael-Leiba, M., Love, D., McCue, K., and Gibson, G., 1994, The Uluru (Ayers Rock), Australia, earthquake of 28 May 1989: Bulletin of the Seismological Society of America, v. 84, no. 1, p. 209–214.
Mohammadi, H., Quigley, M., Steacy, S., and Duffy, B., 2019, Effects of source model variations on Coulomb stress analyses of a multi-fault intraplate earthquake sequence: Tectonophysics, v. 766, p. 151–166, https://doi.org/10.1016/j.tecto.2019.06.007.
Mooney, W.D., Ritsema, J., and Hwang, Y.K., 2012, Crustal seismicity and the earthquake catalog maximum moment magnitude (Mcmax) in stable continental regions (SCRs): Correlation with the seismic velocity of the lithosphere: Earth and Planetary Science Letters, v. 357, p. 78–83, https://doi.org/10.1016/j.epsl.2012.08.032.
Moss, R.E.S., and Ross, Z.E., 2011, Probabilistic fault displacement hazard analysis for reverse faults: Bulletin of the Seismological Society of America, v. 101, no. 4, p. 1542–1553, https://doi.org/10.1785/0120100248.
Oglesby, D., 2008, Rupture termination and jump on parallel offset faults: Bulletin of the Seismological Society of America, v. 98, no. 1, p. 440–447, https://doi.org/10.1785/0120070163.
Oglesby, D.D., 2020, What can surface-slip distributions tell us about fault connectivity at depth?: Bulletin of the Seismological Society of America, v. 110, no. 3, p. 1025–1036, https://doi.org/10.1785/0120190245.
Okubo, P.G., and Aki, K., 1987, Fractal geometry in the San Andreas fault system: Journal of Geophysical Research–Solid Earth, v. 92, no. B1, p. 345–355, https://doi.org/10.1029/JB092iB01p00345.
Perrin, C., Manighetti, I., Ampuero, J.P., Cappa, F., and Gaudemer, Y., 2016, Location of largest earthquake slip and fast rupture controlled by along-strike change in fault structural maturity due to fault growth: Journal of Geophysical Research–Solid Earth, v. 121, no. 5, p. 3666–3685, https://doi.org/10.1002/2015JB012671.
Polcari, M., Albano, M., Atzori, S., Bignami, C., and Stramondo, S., 2018, The causative fault of the 2016 Mwp 6.1 Petermann Ranges intraplate earthquake (Central Australia) retrieved by C- and L-band InSAR data: Remote Sensing, v. 10, no. 8, p. 1311, https://doi.org/10.3390/rs10081311.
Power, W.L., and Tullis, T.E., 1991, Euclidean and fractal models for the description of rock surface-roughness: Journal of Geophysical Research–Solid Earth and Planets, v. 96, no. B1, p. 415–424, https://doi.org/10.1029/90JB02107.
Quigley, M., Van Dissen, R., Litchfield, N., Villamor, P., Duffy, B., Barrell, D., Furlong, K.P., Stahl, T., Bilderback, E., and Noble, D., 2012, Surface rupture during the 2010 Mw 7.1 Darfield (Canterbury) earthquake: Implications for fault rupture dynamics and seismic-hazard analysis: Geology, v. 40, no. 1, p. 55–58, https://doi.org/10.1130/G32528.1.
Quigley, M., Mohammadi, H., Jimenez, A., and Duffy, B.G., 2017, Multi-fault earthquakes with kinematic and geometric rupture complexity: How common, *in* International Union for Quaternary Research (INQUA) Focus Group Earthquake Geology and Seismic Hazards: New Zealand, 8th International INQUA Meeting on Paleoseismology, Active Tectonics and Archeoseismology (PATA), 13–16 November 2017.
Rajabi, M., Tingay, M., Heidbach, O., Hillis, R., and Reynolds, S., 2017, The present-day stress field of Australia: Earth-Science Reviews, v. 168, p. 165–189, https://doi.org/10.1016/j.earscirev.2017.04.003.
Scholz, C.H., and Lawler, T.M., 2004, Slip tapers at the tips of faults and earthquake ruptures: Geophysical Research Letters, v. 31, no. 21, L21609, https://doi.org/10.1029/2004GL021030.
Schueller, S., Gueydan, F., and Davy, P., 2005, Brittle-ductile coupling: Role of ductile viscosity on brittle fracturing: Geophysical Research Letters, v. 32, no. 10, L10308, https://doi.org/10.1029/2004GL022272.
Segall, P., and Pollard, D.D., 1980, Mechanics of discontinuous faults: Journal of Geophysical Research, v. 85, no. B8, p. 4337–4350, https://doi.org/10.1029/JB085iB08p04337.
Shen, Z.K., Sun, J.B., Zhang, P.Z., Wan, Y.G., Wang, M., Burgmann, R., Zeng, Y.H., Gan, W.J., Liao, H., and Wang, Q.L., 2009, Slip maxima at fault junctions and rupturing of barriers during the 2008 Wenchuan earthquake: Nature Geoscience, v. 2, no. 10, p. 718–724, https://doi.org/10.1038/ngeo636.
Starr, A.T., 1928, Slip in a crystal and rupture in a solid due to shear: Proceedings of the Cambridge Philosophical Society, v. 24, p. 489–500.
Stirling, M., McVerry, G., Gerstenberger, M., Litchfield, N., Van Dissen, R., Berryman, K., Barnes, P., Wallace, L., Villamor, P., Langridge, R., Lamarche, G., Nodder, S., Reyners, M., Bradley, B., Rhoades, D., Smith, W., Nicol, A., Pettinga, J., Clark, K., and Jacobs, K., 2012, National Seismic Hazard Model for New Zealand: 2010 update: Bulletin of the Seismological Society of America, v. 102, no. 4, p. 1514–1542, https://doi.org/10.1785/0120110170.
Stockwell, R.G., Mansinha, L., and Lowe, R.P., 1996, Localization of the complex spectrum: The S transform: IEEE Transactions on Signal Processing, v. 44, no. 4, p. 998–1001, https://doi.org/10.1109/78.492555.
Thingbaijam, K.K.S., and Mai, P.M., 2016, Evidence for truncated exponential probability distribution of earthquake slip: Bulletin of the Seismological Society of America, v. 106, no. 4, p. 1802–1816, https://doi.org/10.1785/0120150291.
Wells, D.L., and Coppersmith, K.J., 1994, New empirical relationships among magnitude, rupture length, rupture width, rupture area, and surface displacement: Bulletin of the Seismological Society of America, v. 84, no. 4, p. 974–1002.
Weng, H.H., and Ampuero, J.P., 2019, The dynamics of elongated earthquake ruptures: Journal of Geophysical Research–Solid Earth, v. 124, no. 8, p. 8584–8610, https://doi.org/10.1029/2019JB017684.
Weng, H.H., and Yang, H.F., 2017, Seismogenic width controls aspect ratios of earthquake ruptures: Geophysical Research Letters, v. 44, no. 6, p. 2725–2732, https://doi.org/10.1002/2016GL072168.
Wesnousky, S.G., 2006, Predicting the endpoints of earthquake ruptures: Nature, v. 444, no. 7117, p. 358–360, https://doi.org/10.1038/nature05275.
Wesnousky, S.G., 2008, Displacement and geometrical characteristics of earthquake surface ruptures: Issues and implications for seismic-hazard analysis and the process of earthquake rupture: Bulletin of the Seismological Society of America, v. 98, no. 4, p. 1609–1632, https://doi.org/10.1785/0120070111.
Wessel, P., Smith, W., Scharroo, R., Luis, J., and Wobbe, F., 2013, Generic mapping tools: Improved version released: Eos (Washington, D.C.), v. 94, no. 45, p. 409–410, https://doi.org/10.1002/2013EO450001.
Youngs, R.R., Arabasz, W.J., Anderson, R.E., Ramelli, A.R., Ake, J.P., Slemmons, D.B., McCalpin, J.P., Doser, D.I., Fridrich, C.J., Swan, F.H., Rogers, A.M., Yount, J.C., Anderson, L.W., Smith, K.D., Bruhn, R.L., Knuepfer, P.L.K., Smith, R.B., dePolo, C.M., O'Leary, D.W., Coppersmith, K.J., Pezzopane, S.K., Schwartz, D.P., Whitney, J.W., Olig, S.S., and Toro, G.R., 2003, A methodology for probabilistic fault displacement hazard analysis (PFDHA): Earthquake Spectra, v. 19, no. 1, p. 191–219, https://doi.org/10.1193/1.1542891.
Zhao, S., and Muller, R.D., 2003, Three-dimensional finite-element modelling of the tectonic stress field in continental Australia, *in* Hillis, R.R., and Müller, R.D., eds., Evolution and Dynamics of the Australian Plate: Geological Society of America Special Paper 372, p. 71–89, https://doi.org/10.1130/0-8137-2372-8.71.
Zielke, O., Klinger, Y., and Arrowsmith, J.R., 2015, Fault slip and earthquake recurrence along strike-slip faults—Contributions of high-resolution geomorphic data: Tectonophysics, v. 638, p. 43–62, https://doi.org/10.1016/j.tecto.2014.11.004.
Zinke, R., Hollingsworth, J., and Dolan, J.F., 2014, Surface slip and off-fault deformation patterns in the 2013 MW 7.7 Balochistan, Pakistan, earthquake: Implications for controls on the distribution of near-surface coseismic slip: Geochemistry Geophysics Geosystems, v. 15, no. 12, p. 5034–5050, https://doi.org/10.1002/2014GC005538.

Science Editor: Wenjiao Xiao
Associate Editor: YaJun Hsu

Manuscript Received 30 June 2020
Revised Manuscript Received 28 October 2020
Manuscript Accepted 17 November 2020

Printed in the USA